

## Supplementary Information

### Double self-reinforced coordination modulation constructing stable Ni<sup>4+</sup> for water oxidation

Ya-Nan Zhou <sup>a</sup>, Feng-Ting Li <sup>b</sup>, Bin Dong <sup>\*a</sup>, Yong-Ming Chai <sup>\*a</sup>

<sup>a</sup> *State Key Laboratory of Heavy Oil Processing, College of Science, China University of Petroleum (East China), Qingdao 266580, PR China*

<sup>b</sup> *School of Materials Science and Engineering, China University of Petroleum (East China), Qingdao 266580, PR China*

---

\* Corresponding author. Email: [dongbin@upc.edu.cn](mailto:dongbin@upc.edu.cn) (B. Dong); [ymchai@upc.edu.cn](mailto:ymchai@upc.edu.cn) (Y.M. Chai)

Tel: +86-532-86981156, Fax: +86-532-86981156

## 1 **Experimental Section**

### 2 **Chemicals**

3 Commercial nickel foam (NF) and all chemicals were purchased from Aladdin. NF was  
4 cut into pieces of  $1 \times 2 \text{ cm}^2$  and cleaned with acetone, 3 M HCl, ethanol and deionized water  
5 for 20 min, respectively, to remove stains and oxides from the surface. All reagents used were  
6 analytically pure.

### 7 **Synthesis of NiNH**

8 A 50 ml flask containing 10 g  $\text{Ni}(\text{NO}_3)_2 \cdot 6\text{H}_2\text{O}$  was put into an oven at  $125 \text{ }^\circ\text{C}$  for 20 min  
9 till the salt was totally molted. Then the cleaned NF was dipped into the molten and reacted at  
10  $125 \text{ }^\circ\text{C}$  for 10 h. The obtained NiNH was washed with deionized water and ethanol to remove  
11 the excess  $\text{Ni}(\text{NO}_3)_2 \cdot 6\text{H}_2\text{O}$ .

### 12 **Synthesis of $\text{Co}_x\text{-NiNH}$ , Fe-NiNH and Ru-NiNH**

13 The above NiNH was immersed in  $x \text{ M}$   $\text{Co}(\text{NO}_3)_2 \cdot 6\text{H}_2\text{O}$  at  $80 \text{ }^\circ\text{C}$  for 2 h to synthesize  $\text{Co}_x\text{-}$   
14 NiNH ( $x=0.5, 1.0, 1.5, 2.0$ ). Fe-NiNH and Ru-NiNH were synthesized by replacing  
15  $\text{Co}(\text{NO}_3)_2 \cdot 6\text{H}_2\text{O}$  with  $\text{Fe}(\text{NO}_3)_3 \cdot 9\text{H}_2\text{O}$  and  $\text{RuCl}_3$ , respectively.

### 16 **Synthesis of $\text{Ni}(\text{OH})_2$**

17 To prepare  $\text{Ni}(\text{OH})_2$ , 1.830 g  $\text{Ni}(\text{NO}_3)_2 \cdot 6\text{H}_2\text{O}$ , 0.148 g  $\text{NH}_4\text{F}$  and 1.201 g urea dissolved in  
18 72 ml deionized water with continuous stirring. The olive solution and a piece of NF were  
19 transformed into a stainless steel reaction kettle with a Teflon lining and heated it at  $120 \text{ }^\circ\text{C}$  for  
20 6 h. After cooling down to room temperature naturally, the sample was washed with deionized  
21 water and named  $\text{Ni}(\text{OH})_2$ .

### 22 **Synthesis of $\text{Co}_x\text{-Ni}(\text{OH})_2$**

1 The synthesis method of  $\text{Co}_x\text{-Ni(OH)}_2$  is similar to that of  $\text{Co}_x\text{-NiNH}$  except that NiNH is  
2 replaced by  $\text{Ni(OH)}_2$ .

### 3 **Material characterizations**

4 Scanning electron microscopy (SEM) and X-ray energy spectrometer (EDS) were taken on  
5 JEOL JSM-6490 field emission scanning electron microscope operated at 5 kV with EDS  
6 detector. Stick the conductive adhesive on the sample holder. The sample to be ground into  
7 powder was then sprinkled evenly on it. The unbonded powder was blown off with a rubber  
8 suction bulb to obtain the SEM sample. Transmission electron microscope (TEM) and high-  
9 resolution TEM (HRTEM) were collected on FEI Tecnai G2 F30 with an accelerating voltage  
10 of 200 kV. First, the fully ground sample was dispersed into an ethanol solution, homogenized  
11 by ultrasonic shock, and then the droplets were placed on the copper mesh covered with carbon  
12 film with a pipette. After drying at room temperature, TEM samples were prepared. The TEM  
13 studies were conducted at an operating voltage of 200 kV. X-ray diffraction (XRD) patterns  
14 were recorded by using a Rigaku D/max-2500PC X-ray diffractometer with  $\text{Cu-K}\alpha$  radiation  
15 ( $\lambda = 1.5418 \text{ \AA}$ ). X-ray photoelectron spectroscopy (XPS) was collected on a Thermo Scientific  
16 Escalab 250Xi X-ray photoelectron spectrometer, using non-monochromatized  $\text{Al-K}\alpha$  X-ray  
17 (1486.6 eV) as the excitation source. Binding energies reported herein are referenced to C (1s)  
18 at 284.5 eV. Raman measurement was performed on the LabRAM HR Evolution with the  
19 excitation wavelength of 532 nm. Electron paramagnetic resonance (EPR) was recorded by  
20 using MS5000. Fourier transform infrared spectroscopy (FTIR) measurements were conducted  
21 on Thermo Fisher-Nicolet 6700. Photoluminescence (PL) was detected by the OmniPL-MicroS  
22 microscopic photoluminescence spectroscopy system with an excitation light of 325 nm. In the

1 WITEC alpha300R confocal microprobe Raman system, electrochemical in-situ Raman  
2 spectroscopy was recorded using a 532 nm laser with a power of approximately 17 mW. The  
3 Raman frequency was calibrated using Si wafers. In situ Raman spectroscopy measurements  
4 were carried out with a Pt plate and Hg/HgO using customized electrochemical cells. The  
5 electrolyte was 1 M KOH. To monitor the evolution of catalyst samples during OER, Raman  
6 spectra were collected after the constant potential was applied to the catalyst electrode for 10  
7 min. The collection time of each spectrum was 30 s with accumulating 5 times. Brunner-  
8 Emmet-Teller (BET) measurements were conducted with a 3H-2000BET-A BET-specific  
9 surface area tester.

## 10 **Electrochemical measurements**

11 All of the electrochemical measurements for OER were performed using a Gamry interface  
12 1000 electrochemical workstation in a standard three-electrode electrochemical cell with O<sub>2</sub>-  
13 saturated 1M KOH solution as electrolyte<sup>1</sup>. The as-prepared NiNH, Co<sub>x</sub>-NiNH, Ni(OH)<sub>2</sub> and  
14 Co<sub>x</sub>-Ni(OH)<sub>2</sub> samples were used as working electrode. A Pt plate and Hg/HgO (1M KOH)  
15 served as counting electrode and reference electrode, respectively. The measured potential was  
16 converted to the potential versus reversible hydrogen electrode (RHE):  $E_{RHE} = E_{Hg/HgO} + 0.098$   
17  $+0.059pH$ . Several CV scanning cycles were performed to stabilize the catalysts before the  
18 electrochemical performance was assessed. Linear sweep voltammetry (LSV) polarization  
19 curves were measured at a sweep rate of 5 mV s<sup>-1</sup>, and the potentials were corrected by 80%-  
20 iR compensation to eliminate the effect of solution resistance. The Tafel plots were obtained by  
21 the corresponding LSV polarization

22 The stability assessments were performed by chronopotentiometry for 100 h at the current



1 density of 100→200 mA cm<sup>-2</sup> and CV scanning for 3000 cycles in the potential region from 0.0  
2 to 0.3 V versus E<sub>RHE</sub> at a sweep rate of 40 mV s<sup>-1</sup>. C<sub>dl</sub> was determined from the CV scanning  
3 curves measured in the non-Faradaic potential range. C<sub>dl</sub> was estimated by plotting the ΔJ = (J<sub>+</sub>  
4 - J<sub>-</sub>) / 2 at specific potential. ECSA was calculated by the following equation:

$$5 \quad \text{ECSA} = C_{dl} / C_s \times A$$

6 Where C<sub>s</sub> is the specific capacitance of planar surface with atomically smooth under identical  
7 electrolyte conditions (the general value is 40 μF cm<sup>-2</sup>)<sup>2</sup>. EIS was carried out in ZAHNER  
8 Electrochemical workstation with a frequency ranging from 10<sup>-2</sup> to 10<sup>5</sup> Hz with an amplitude  
9 of 5 mV. To assess the intrinsic activity of as-obtained samples, both mass activities and TOFs  
10 were calculated by equations:

$$11 \quad \text{Mass activity} = (j \times A) / m$$

$$12 \quad \text{TOF} = (j \times A) / (4 \times F \times n)$$

13 Where j was the current density, A was the geometric area of electrode, F was the Faraday  
14 constant (96485 C mol<sup>-1</sup>), m was the loading mass of sample, and n was the number of active  
15 sites. Only the Co and Ni atoms were considered as the active sites. In addition, single-cell  
16 anion exchange membrane water electrolyzer was also used for OER performance measurement.  
17 The related experimental setup images are shown in [Fig. S53](#).

18 In some reports<sup>3</sup>, the KOH electrolyte was purified to study the influence of Fe impurities  
19 on OER measurement. 2 g Ni(NO<sub>3</sub>)<sub>2</sub>·6H<sub>2</sub>O was placed in a polypropylene centrifuge tube  
20 washed with H<sub>2</sub>SO<sub>4</sub>. Then, 5 mL of 1 M KOH solution was added. The mixture was shaken and  
21 centrifuged to obtain Ni(OH)<sub>2</sub> precipitate. Then, 2 ml 1M KOH and 20 mL of water were added  
22 to the centrifuge tube, and Ni(OH)<sub>2</sub> precipitate was re-dispersed and centrifuged, and the

1 supernatant was decanted. In this way,  $\text{Ni}(\text{OH})_2$  was repeatedly washed three times. Finally, 50  
2 ml of 1 M KOH was injected into the centrifuge tube. The mixture was mechanically stirred for  
3 at least 10 minutes, allowed to stand for 4 hours and centrifuged. Before storage, the purified  
4 KOH supernatant was poured into a polypropylene bottle washed with  $\text{H}_2\text{SO}_4$ . The Fe content  
5 in unpurified KOH is  $32.1 \mu\text{g L}^{-1}$ . After purification of KOH, Fe content is only  $5.6 \mu\text{g L}^{-1}$ .

6 The Faraday efficiency of the electrode was evaluated by volume method. In detail,  $\text{O}_2$   
7 generated by  $\text{Co}_{0.15}\text{-NiNH}$  electrode (effective area is  $2.0 \text{ cm}^{-2}$ ) is accumulated in a measuring  
8 cylinder filled with deionized water. Under the environmental conditions ( $20^\circ\text{C}$ , 1 atm), the  
9 current of  $100 \text{ mA cm}^{-2}$  is dominant in electrolysis. Record the time every 1ml  $\text{O}_2$ . Meanwhile,  
10 the charge collected by the working electrode is calculated by current  $\times$  time.

## 11 **Theoretical simulations**

12 DFT simulations were performed with the Vienna ab initio simulation package (VASP)<sup>4,5</sup>.  
13 The generalized gradient approximation (GGA) of the Perdew-Burke-Ernzerhof (PBE)  
14 functional and the projector augmented-wave (PAW) potential were employed<sup>6-8</sup>. NiOOH and  
15  $\text{NO}_3^-$ -inserted NiOOH (N-NiOOH) were selected as our model to compare the proton transfer.  
16 Moreover, NiOOH with  $\text{NO}_3^-$  adsorption was modeled and named as (NiOOH-N). On the basis  
17 of NiOOH-N, Co was introduced to obtain the Co-NiOOH-N model with a (4 $\times$ 4) supercell. The  
18 periodic boundary condition (PBC) was set with a 20 Å vacuum region above the surface to  
19 avoid the attractions from adjacent periodic mirror images.  $\text{Co}(\text{OH})_2$  with the (10-14) crystal  
20 face was constructed. Based on it,  $\text{NO}_3^-$ -inserted  $\text{Co}(\text{OH})_2$  (N- $\text{Co}(\text{OH})_2$ ) was built using a (4 $\times$ 4)  
21 supercell to study the OER process. Structures were relaxed until all forces on each atom were  
22 less than  $0.01 \text{ eV}/\text{Å}$ . The convergence criterion for electronic iteration was  $10^{-6} \text{ eV}$ .

1 The computational hydrogen electrode (CHE) model was applied to simulate the OER  
2 pathway and determine the reaction energy barrier for different slab models<sup>9-11</sup>. Various oxygen  
3 species intermediates were considered and the related adsorption energy ( $\Delta E_{\text{ads}}$ ) of those  
4 intermediates was calculated according to the relationship:

$$5 \quad \Delta E_{\text{ads}} = E_{\text{total}} - E_{\text{sub}} - E_{\text{ads}}$$

6 Where the  $E_{\text{total}}$ ,  $E_{\text{sub}}$  and  $E_{\text{ads}}$  are the total energies of the systems, the substrates, and the  
7 adsorbates, respectively. The Gibbs free energy change ( $\Delta G$ ) of each step was defined as:

$$8 \quad \Delta G = \Delta E - \Delta \text{ZPE} - (-T\Delta S)$$

9 where  $\Delta E$  is the electronic energy difference,  $\Delta \text{ZPE}$  and  $\Delta S$  are the difference of zero-point  
10 energies and the change of entropy, respectively, which were estimated from the vibrational  
11 frequencies, and  $T = 298.15 \text{ K}$ .

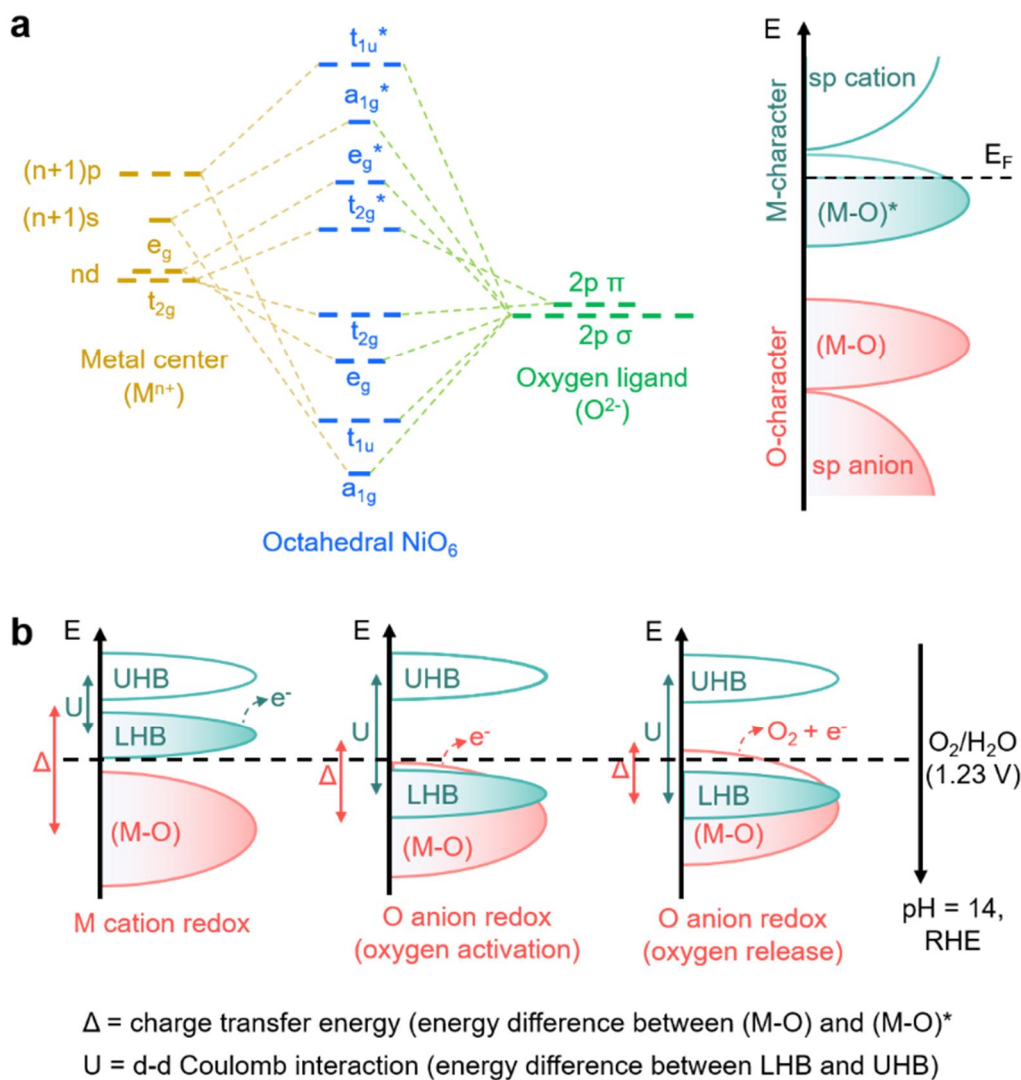
12 The hydrogen desorption energy (HDE) was calculated as:

$$13 \quad E_{\text{HDE}} = E_{\text{H}(n-1)} - E_{\text{Hn}} + 1/2 E(\text{H}_2)$$

14 Where the  $E_{\text{H}(n-1)}$  and  $E_{\text{Hn}}$  are the total DFT energies for the Ni hydroxides systems.  $E(\text{H}_2)$   
15 is the total energy of  $\text{H}_2$ .

16

17



1  
 2 **Fig. S1.** The relationship between electronic structure and OER mechanism. (a) The schematic  
 3 band structure of octahedral-symmetric  $\text{TMO}_6$  in TMOs under the rationalization of molecular  
 4 orbital theory. (b) The schematic representations of cation/anion redox chemistry guided by d-  
 5 d Coulomb interaction ( $U$ ) and charge transfer energy ( $\Delta$ ), which manifest conventional metal  
 6 cation oxidation (left), oxygen anion oxidation (middle) and direct oxygen anion release (right)  
 7 for OER, respectively.

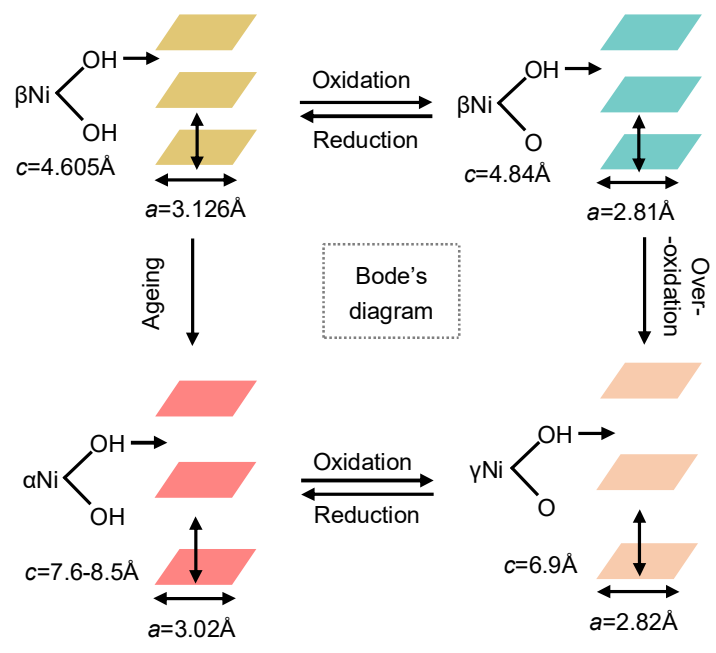


**Fig. S2.** Schematic illustration of the active material transition of nickel hydroxide.

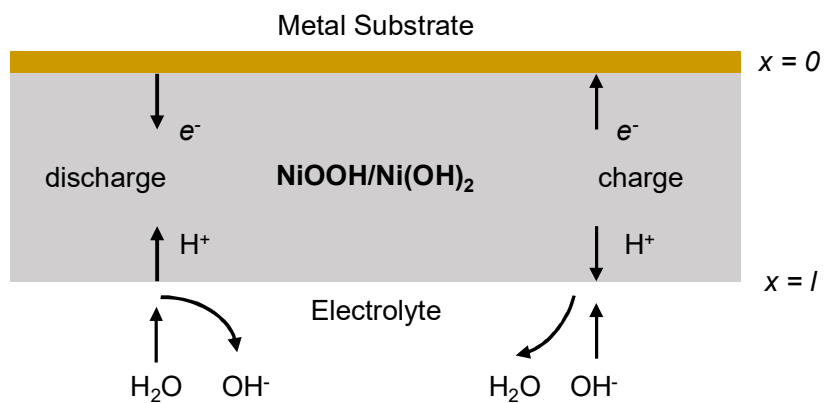


**Fig. S3.** A schematic of a nickel hydroxide film with thickness  $l$  deposited on a conducting substrate. Also shown is the transport of the species involved during charge and discharge.

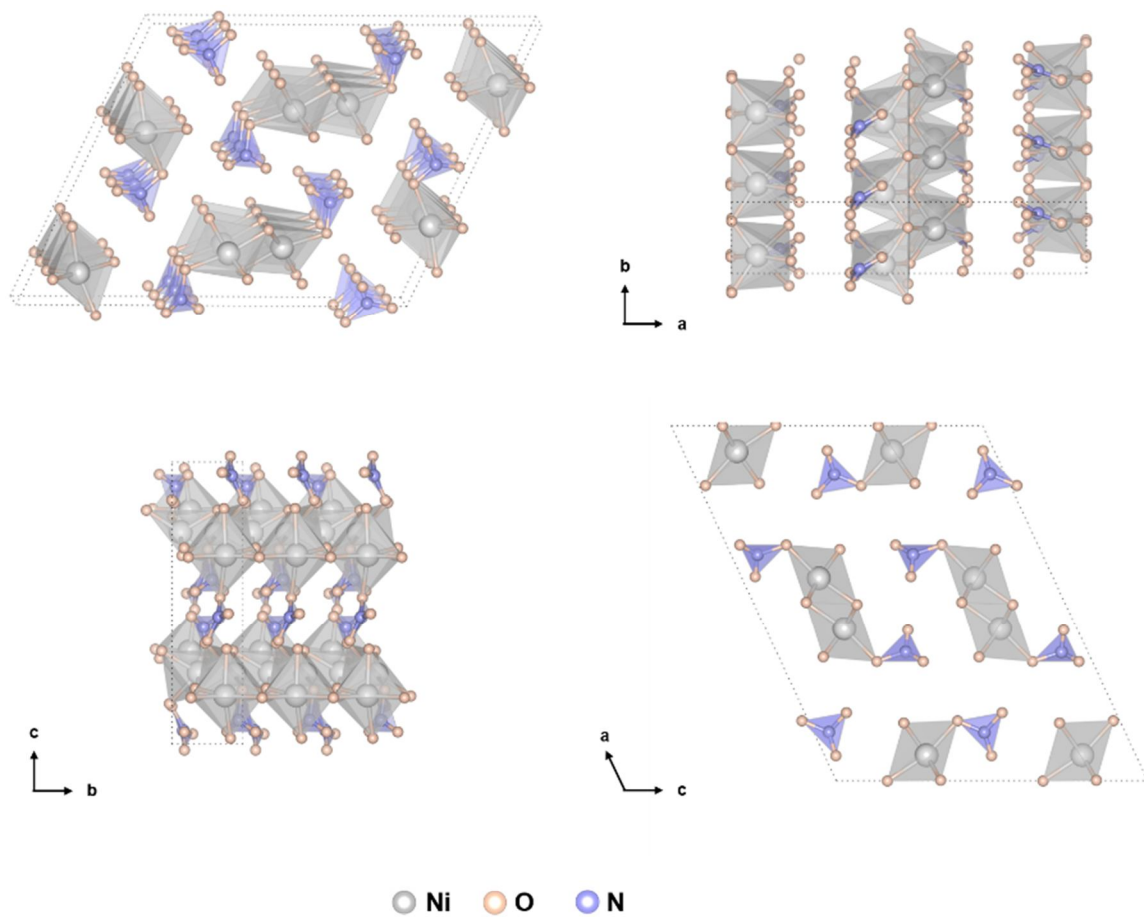


**Fig. S4.** Crystal structure of nickel hydroxynitrate (upper left) and corresponding structure at different view.

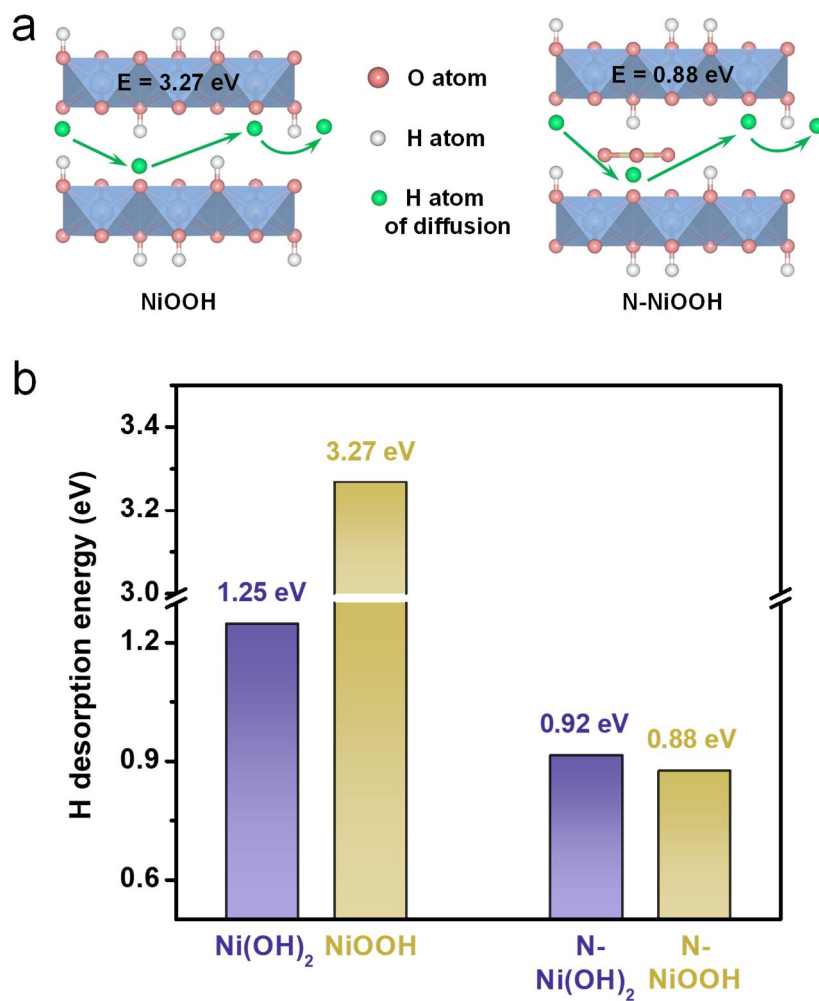


**Fig. S5.** (a) Schematic diagram of Hydrogen desorption, taking NiOOH and NO<sub>3</sub><sup>-</sup> inserted NiOOH (N-NiOOH) as examples. (b) Hydrogen desorption energy for Ni(OH)<sub>2</sub>, N-Ni(OH)<sub>2</sub>, NiOOH and N-NiOOH.



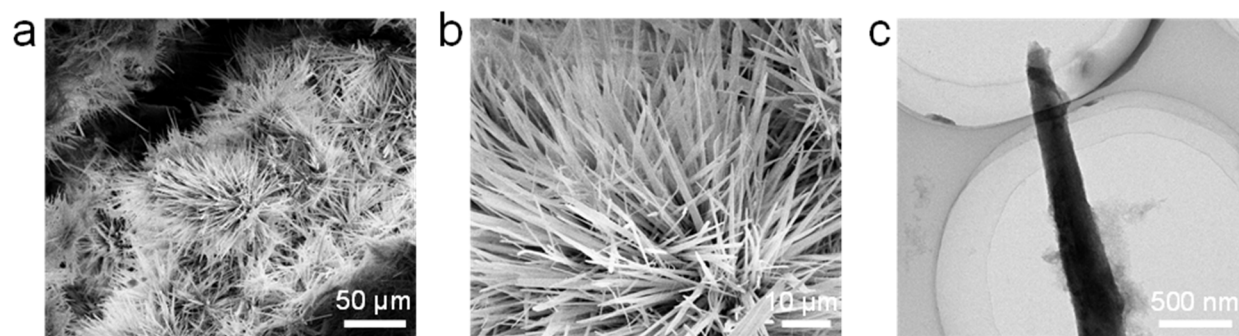


**Fig. S6.** (a,b) SEM images and (c) TEM image of NiNH.

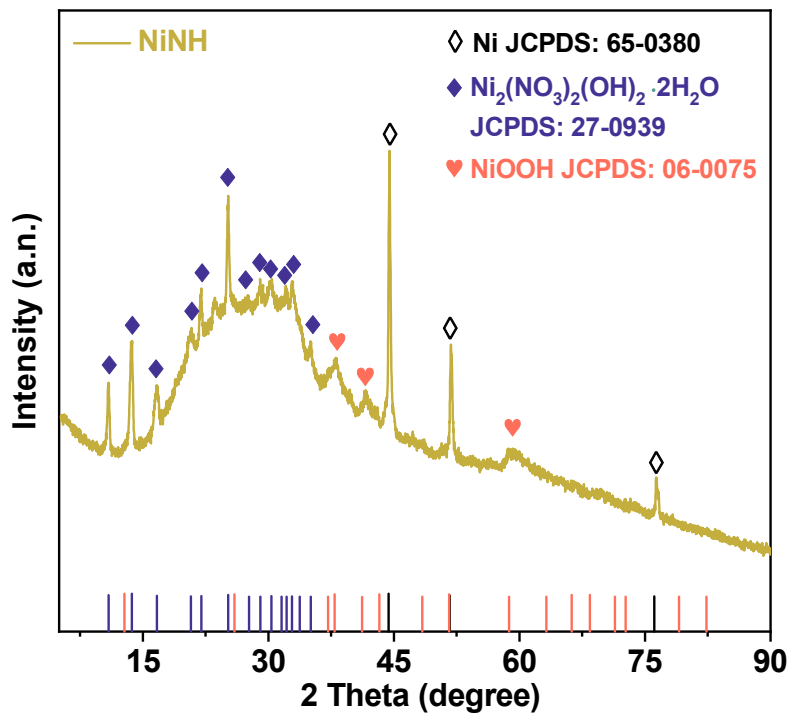
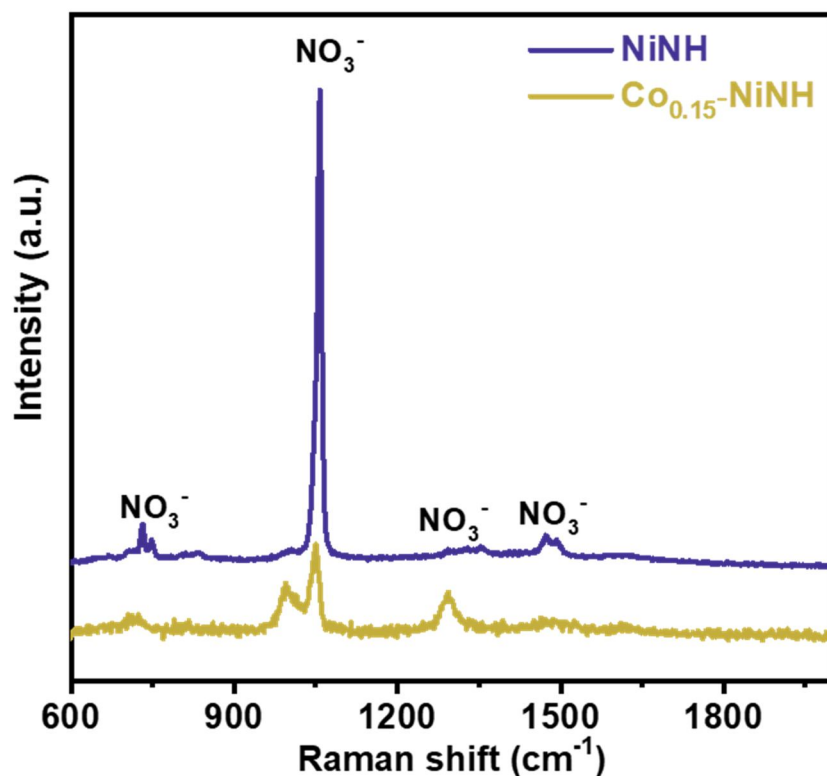


Fig. S7. XRD pattern of NiNH precursor

**Table S1.** Element contains of Co, Ni, N, O in NiNH and Co<sub>0.15</sub>-NiNH.

Element	NiNH		Co <sub>0.15</sub> -NiNH	
	EDS	XPS	EDS	XPS
Co	-	-	3.34	3.87
Ni	14.52	16.94	12.96	11.99
N	13.61	16.35	15.14	14.73
O	71.87	66.71	68.56	69.41
Total amount	100.00	100.00	100.00	100.00



**Fig. S8.** Raman spectra of NiNH and Co<sub>0.15</sub>-NiNH. Peaks at 1472, 1292, 1058 and 731 cm<sup>-1</sup> belong to the NO<sub>3</sub><sup>-</sup>. Among them, peak at 1472 cm<sup>-1</sup> indicates the N-O stretching. Peaks at 1292 and 731 cm<sup>-1</sup> show the antisymmetric stretching vibration of O-N-O. Peak at 1058 cm<sup>-1</sup> presents the symmetric stretching vibration of O-N-O. More importantly, the Raman peaks show obvious splits with the band interval of splitting peak of 18 cm<sup>-1</sup>. Besides, among the three stretching vibration peaks of NiNH and Co<sub>0.15</sub>-NiNH, the middle peak has the strongest intensity. These two characteristics indicate that NO<sub>3</sub><sup>-</sup> is monodentate, that is, an oxygen atom is coordinated with metal Ni. The peak strength at 1058 cm<sup>-1</sup> decreased significantly after Co-doping, which was due to the transfer of the coordination mode of NO<sub>3</sub><sup>-</sup> from single-tooth coordination to double-tooth coordination.

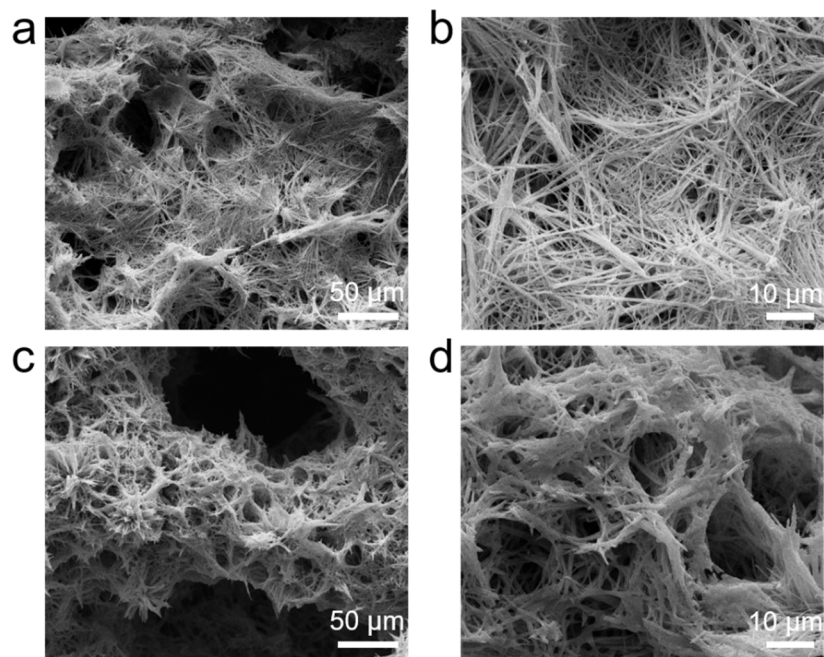


**Fig. S9.** SEM images of (a,b)  $\text{Co}_{0.05}\text{-NiNH}$  and (c,d)  $\text{Co}_{0.20}\text{-NiNH}$ .

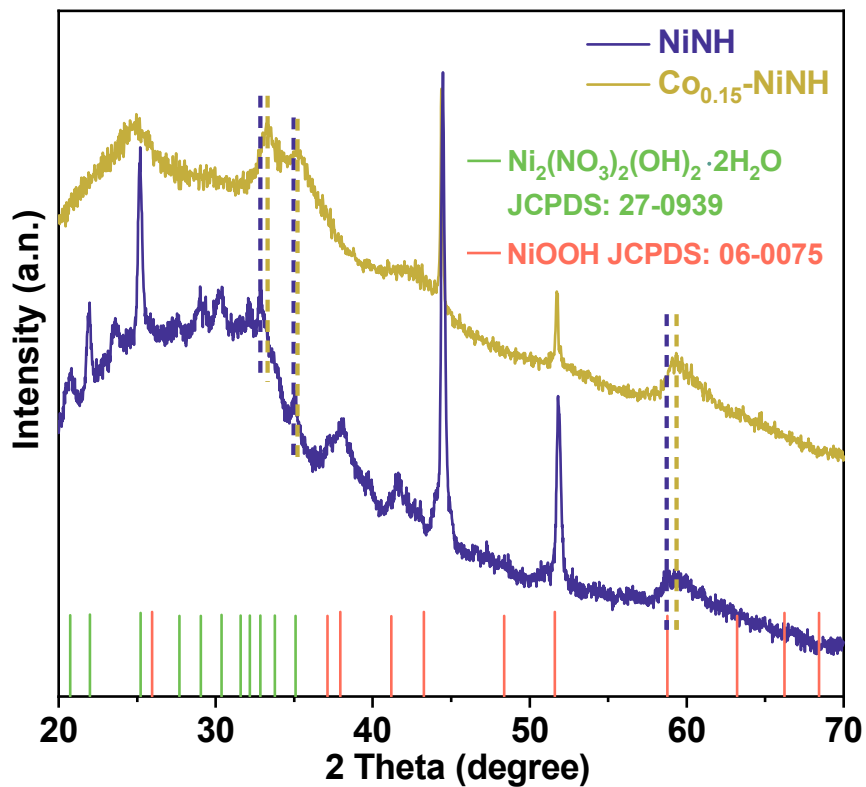


**Fig. S10.** XRD of NiNH and  $\text{Co}_{0.15}\text{-NiNH}$ . The XRD peaks of  $\text{Co}_{0.15}\text{-NiNH}$  shift to a higher degree after Co doping. It is noted that after doping, the XRD peak at 25 degree moves to a low angle, which is due to the existence of micro-strain, resulting in the subgrain being elongated.

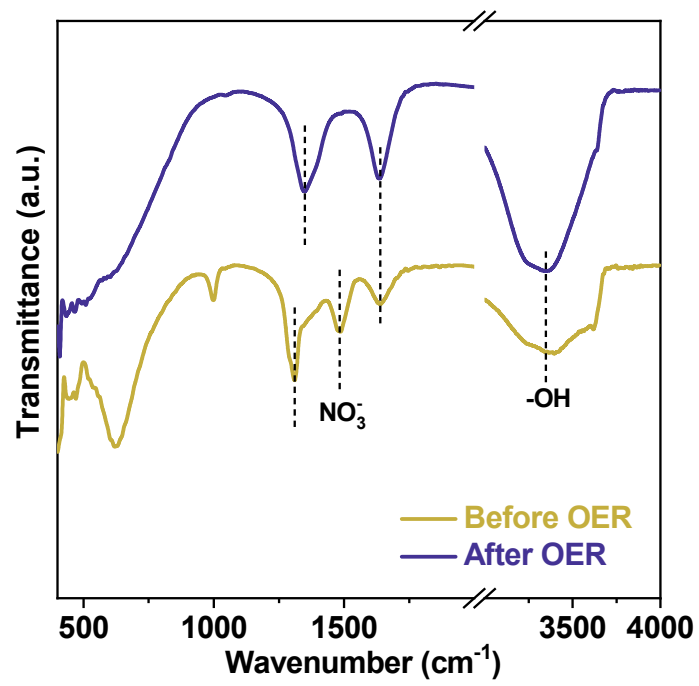


**Fig. S11.** FTIR pattern of Co<sub>0.15</sub>-NiNH before and after OER.

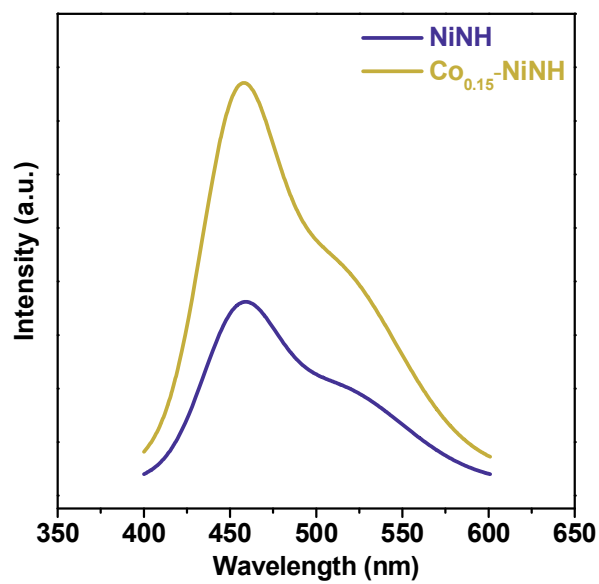


**Fig. S12.** PL signal of NiNH and Co<sub>0.15</sub>-NiNH. The strong peak for Co<sub>0.15</sub>-NiNH means more defects after Co doping considering that the luminescence center is usually composed of impurity ions or lattice defects.



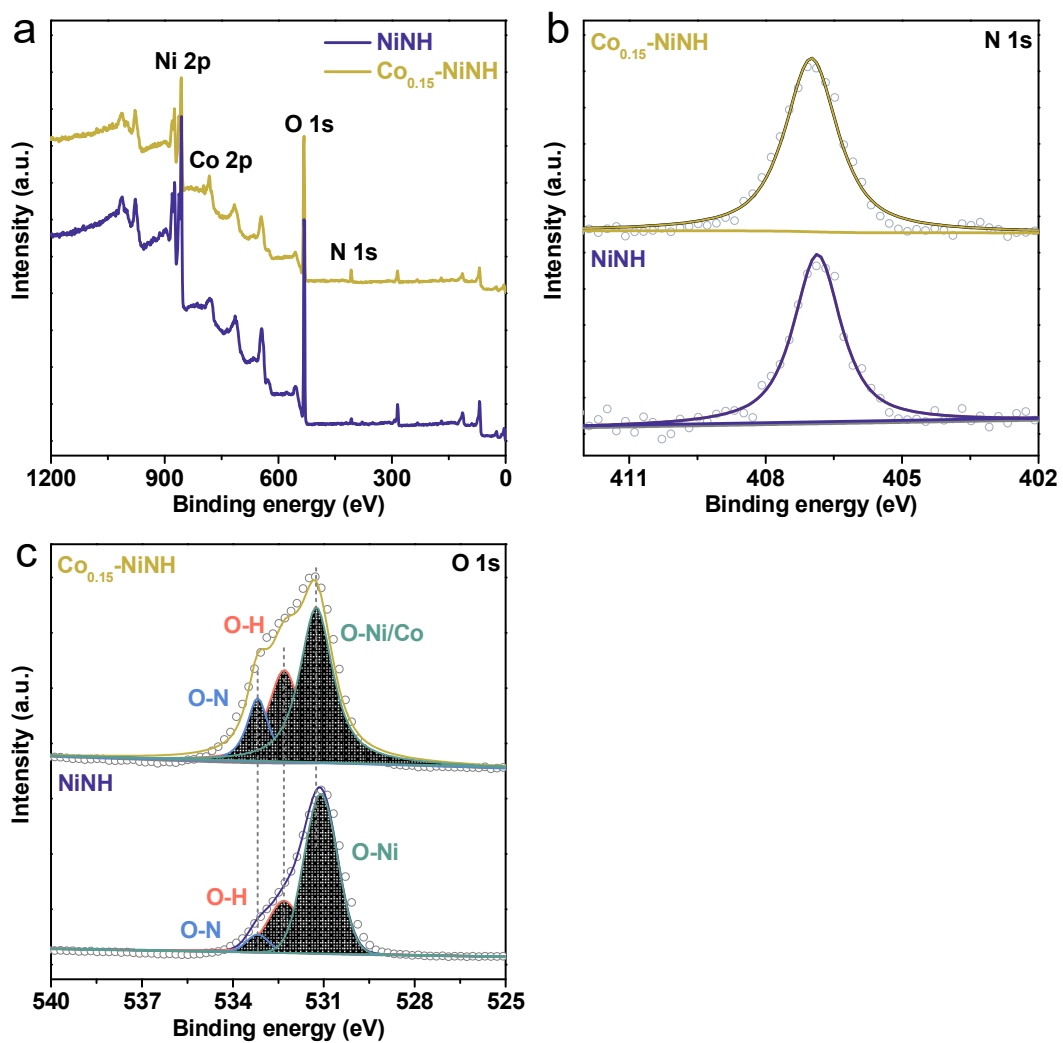
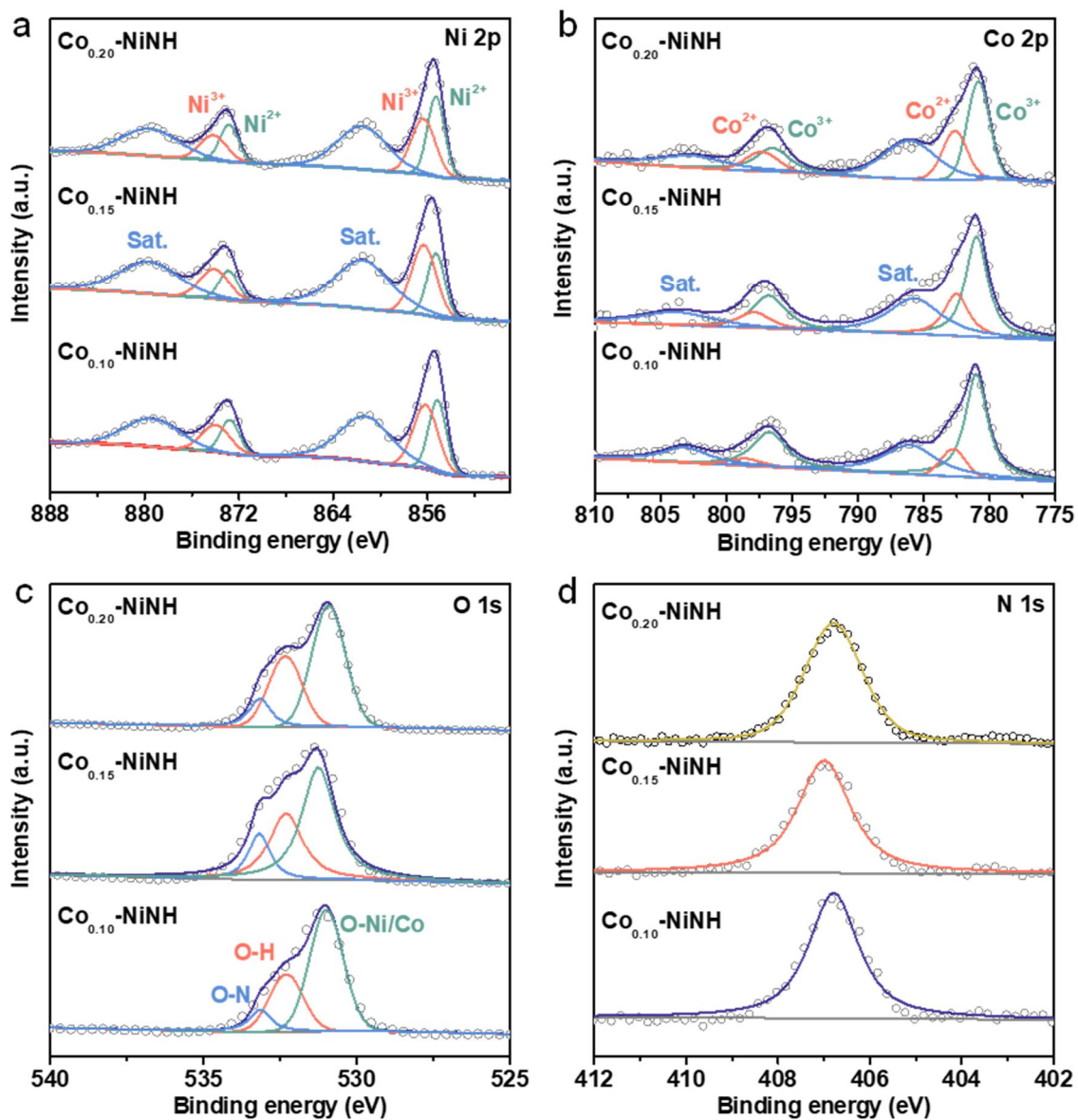
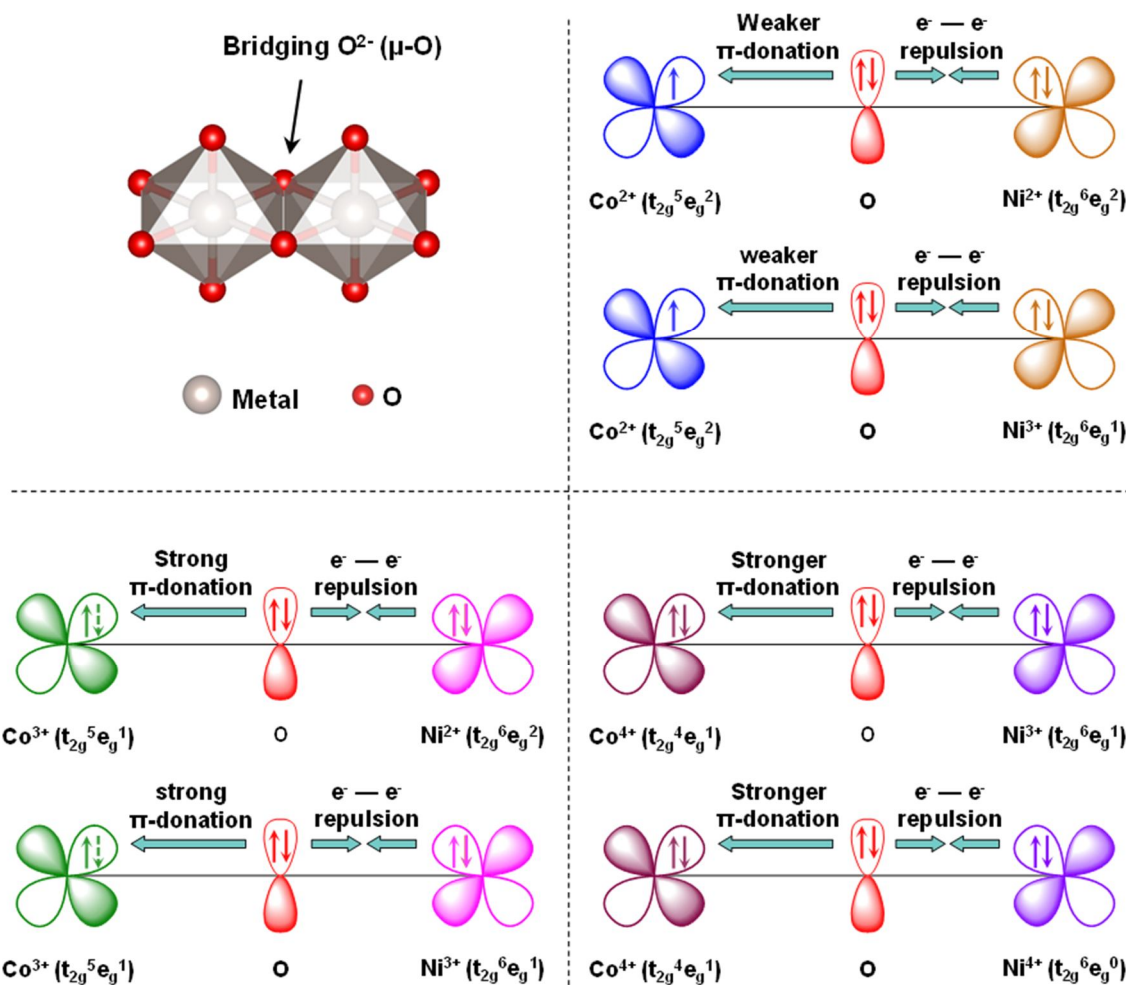


Fig. S13. XPS of NiNH and  $\text{Co}_{0.15}\text{-NiNH}$ . (a) survey scan, (b) N 1s and (c) O1s.



**Fig. S14.** XPS of  $\text{Co}_{0.10}\text{-NiNH}$ ,  $\text{Co}_{0.15}\text{-NiNH}$  and  $\text{Co}_{0.20}\text{-NiNH}$ . (a) Ni 2p, (b) Co 2p and (c) O1s and (d) N 1s.



**Fig. S15.** Schematic representation of two  $\mu$ -bridged MO<sub>6</sub> octahedrons in layered metal (oxy)hydroxide structure and corresponding schematic representations of PET in moieties Co<sup>2+</sup>-O-Ni<sup>2+</sup>, Co<sup>2+</sup>-O-Ni<sup>3+</sup>, Co<sup>3+</sup>-O-Ni<sup>2+</sup>, Co<sup>3+</sup>-O-Ni<sup>3+</sup>, Co<sup>4+</sup>-O-Ni<sup>3+</sup> and Co<sup>4+</sup>-O-Ni<sup>3+</sup> through bridging O ( $\mu$ -O) atom, respectively, where left metal atom serves as the electron acceptor.

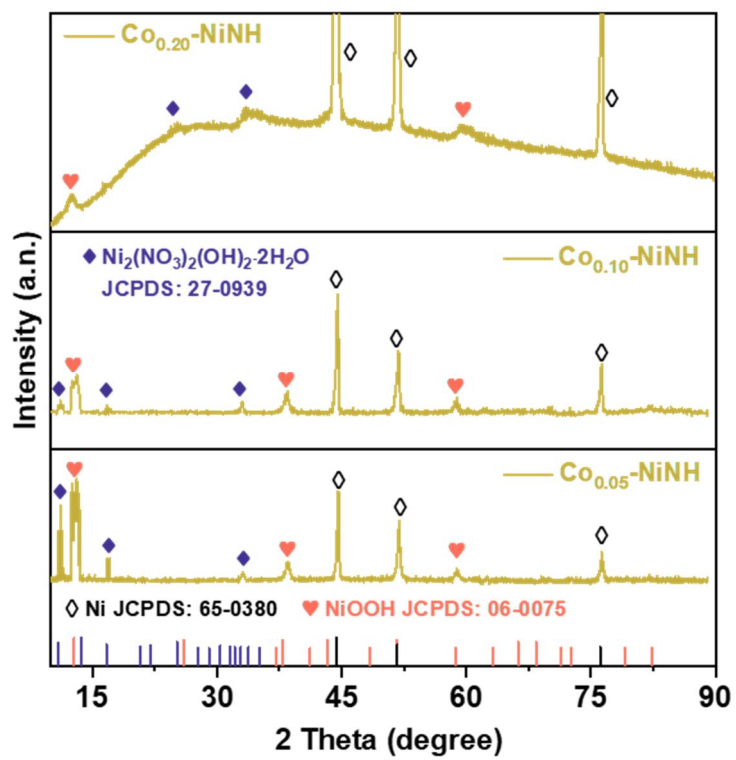


**Fig. S16.** XRD patterns of Co<sub>0.05</sub>-NiNH, Co<sub>0.10</sub>-NiNH and Co<sub>0.20</sub>-NiNH.

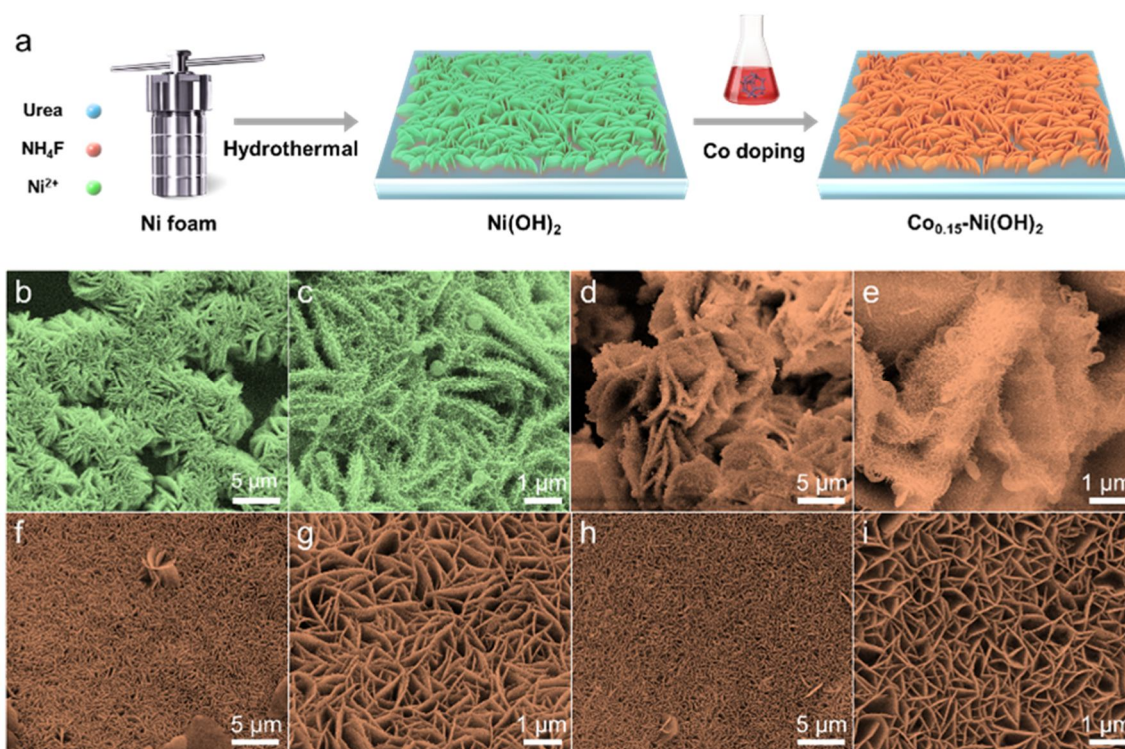


**Fig. S17.** (a) Schematic illustration of synthesis of  $\text{Co}_{0.15}\text{-Ni}(\text{OH})_2$ . SEM images of (b,c)  $\text{Ni}(\text{OH})_2$ , (d,e)  $\text{Co}_{0.10}\text{-Ni}(\text{OH})_2$ , (f,g)  $\text{Co}_{0.15}\text{-Ni}(\text{OH})_2$  and (h,i)  $\text{Co}_{0.20}\text{-Ni}(\text{OH})_2$ .

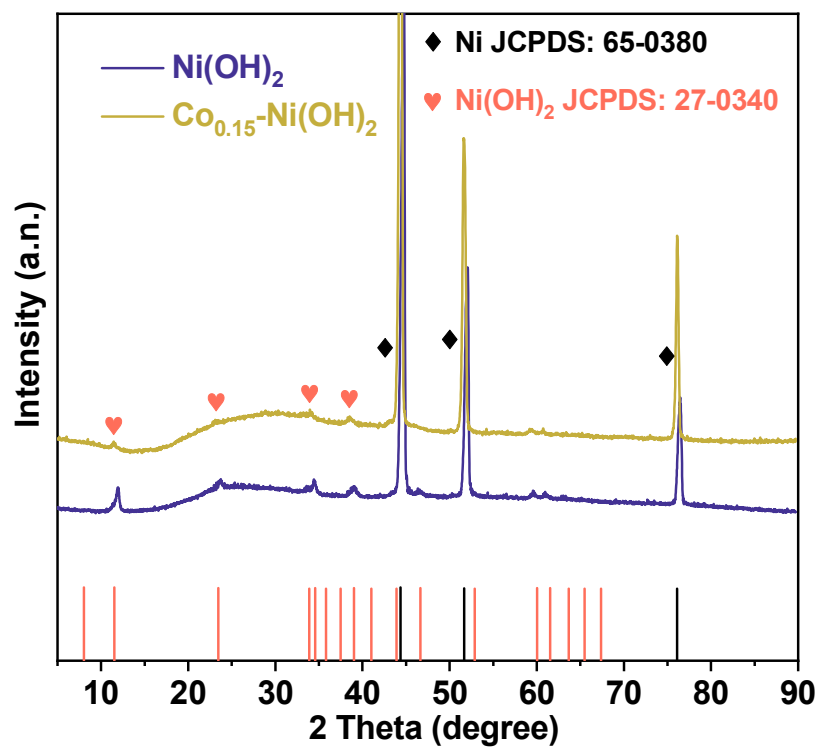
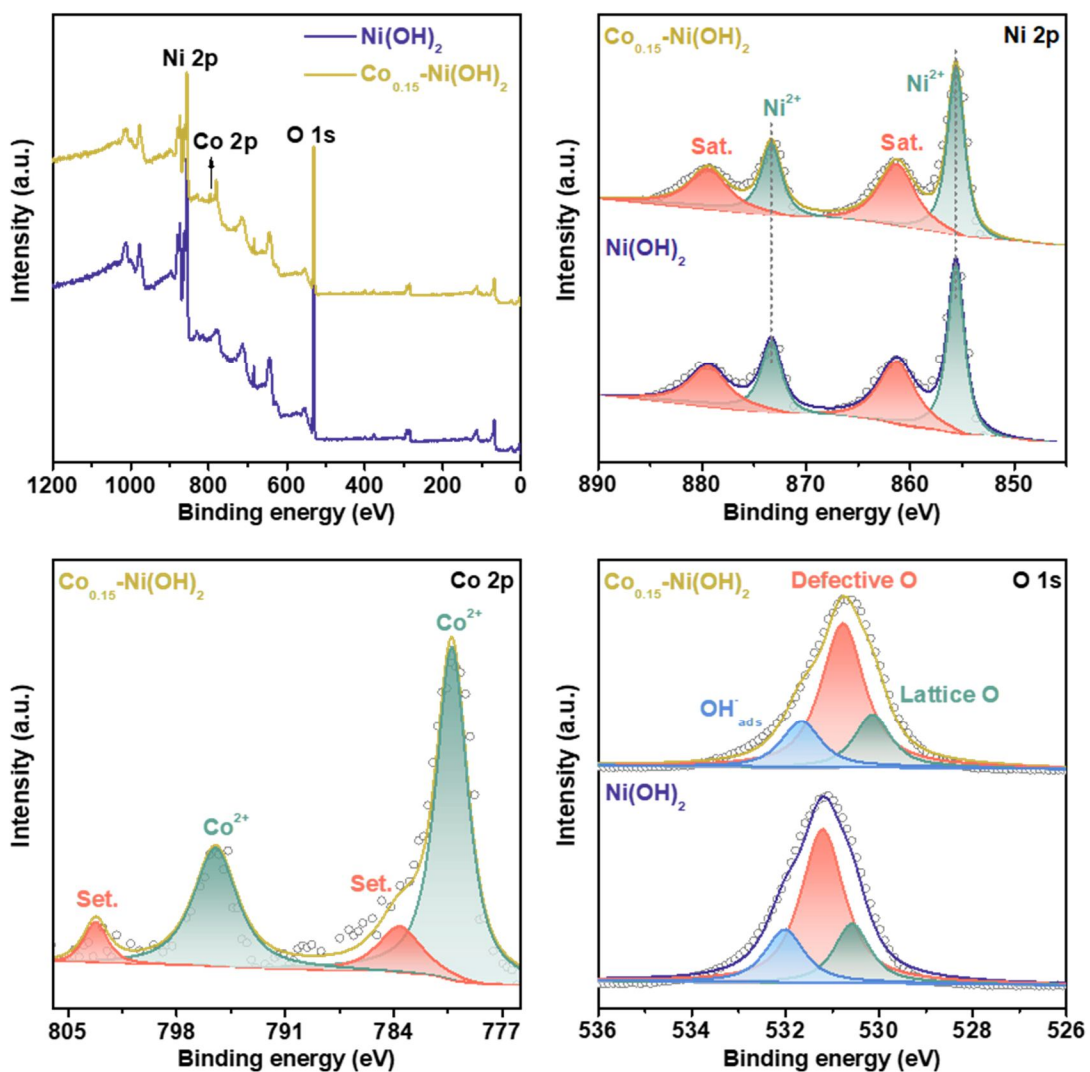
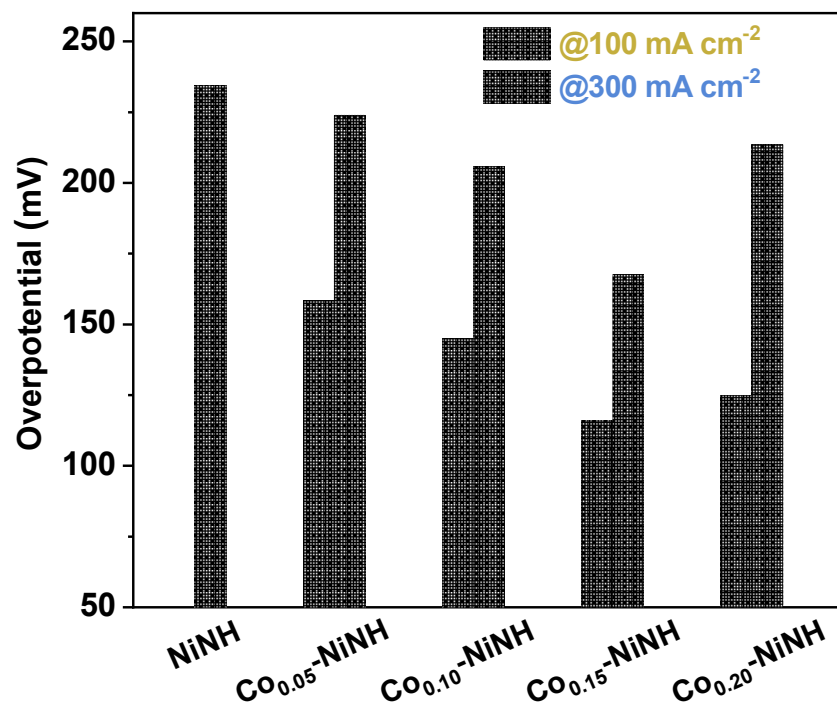


Fig. S18. XRD pattern of  $\text{Ni(OH)}_2$  and  $\text{Co}_{0.15}\text{-Ni(OH)}_2$ .



**Fig. S19.** XPS of  $\text{Ni(OH)}_2$  and  $\text{Co}_{0.15}\text{-Ni(OH)}_2$ . (a) survey scan, (b) Ni 2p, (c) Co 2p and (d) O 1s.



**Fig. S20.** Overpotential at 100 and 300 mA cm<sup>-2</sup> for obtained samples. Specific overpotential values can be obtained in Table S2.



**Table S2.** Overpotential ( $\eta$ ) at 100 and 300 mA cm<sup>-2</sup> for obtained samples. A more visual bar graph is shown in Fig. S20.

Sample	$\eta@100$ mA cm <sup>-2</sup>	$\eta@300$ mA cm <sup>-2</sup>
NiNH	234.5	-
Co <sub>0.05</sub> -NiNH	158.4	224.3
Co <sub>0.10</sub> -NiNH	145.0	204.0
Co <sub>0.15</sub> -NiNH	115.8	167.7
Co <sub>0.20</sub> -NiNH	124.8	213.7

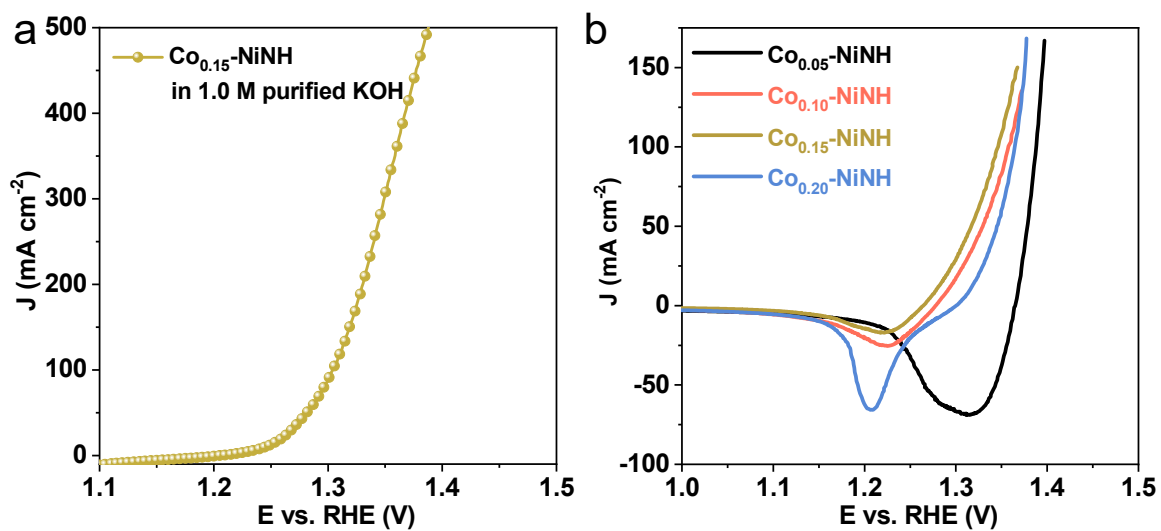


**Fig. S21.** (a) LSV plot of  $\text{Co}_{0.15}\text{-NiNH}$  in 1.0 M purified KOH. (b) LSV curves from CV scanning of  $\text{Co}_{0.05}\text{-NiNH}$ ,  $\text{Co}_{0.10}\text{-NiNH}$ ,  $\text{Co}_{0.15}\text{-NiNH}$  and  $\text{Co}_{0.20}\text{-NiNH}$  in 1.0 M KOH.

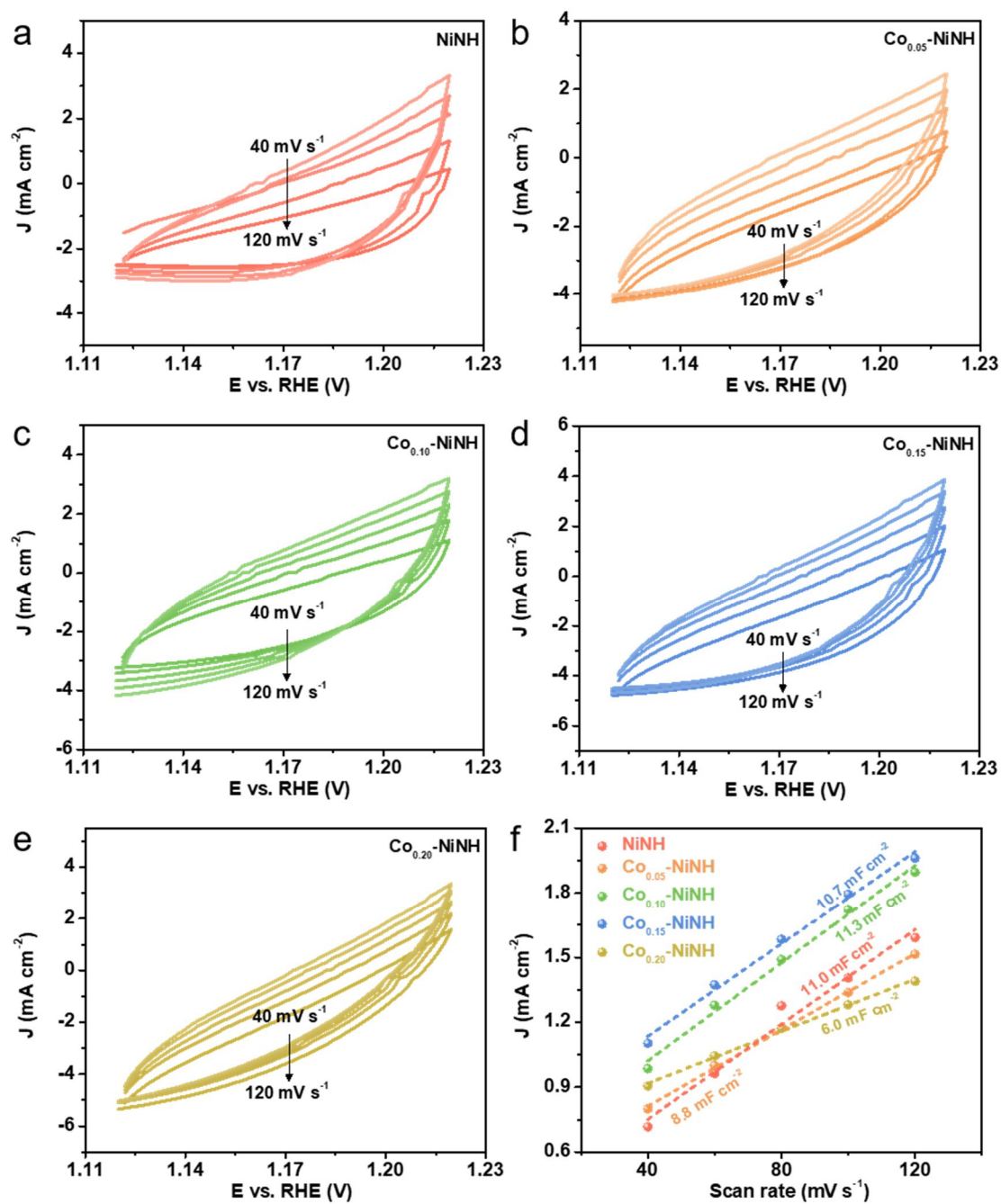


**Fig. S22.** (a-e) CV curves of NiNH and Co-doped NiNH with the scan rate of 40, 60, 80, 100 and 120 mV dec<sup>-1</sup>. (f) The calculated  $C_{dl}$ .

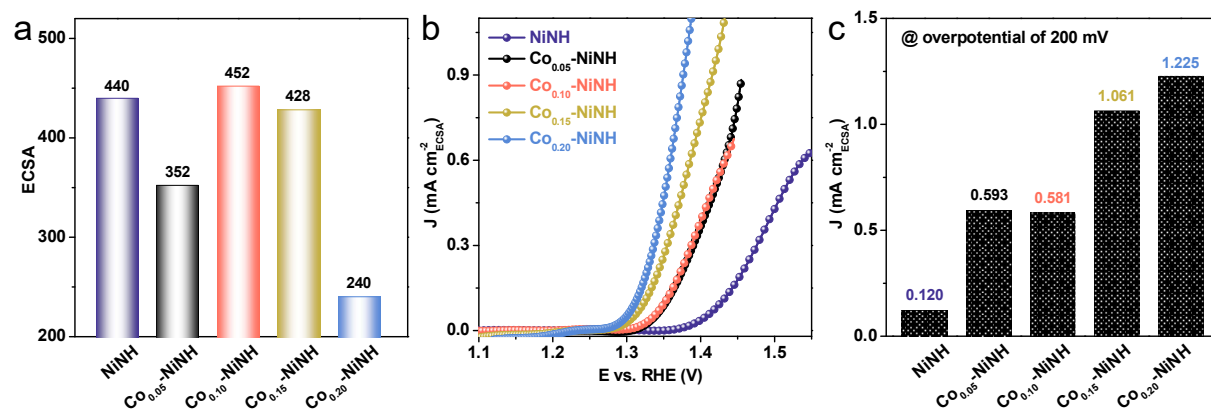


**Fig. S23.** (a) ECSA, (b) ECSA-normalized LSV, (c) Current density at overpotential of 200 mV for NiNH and Co-doped NiNH samples. It is worth noting that although the ECSA of Co<sub>0.15</sub>-NiNH is smaller than NiNH and Co<sub>0.10</sub>-NiNH, it still shows the best ECSA normalization performance, suggesting that the activity enhancement of Co<sub>0.15</sub>-NiNH mainly comes from the improvement of intrinsic activity.

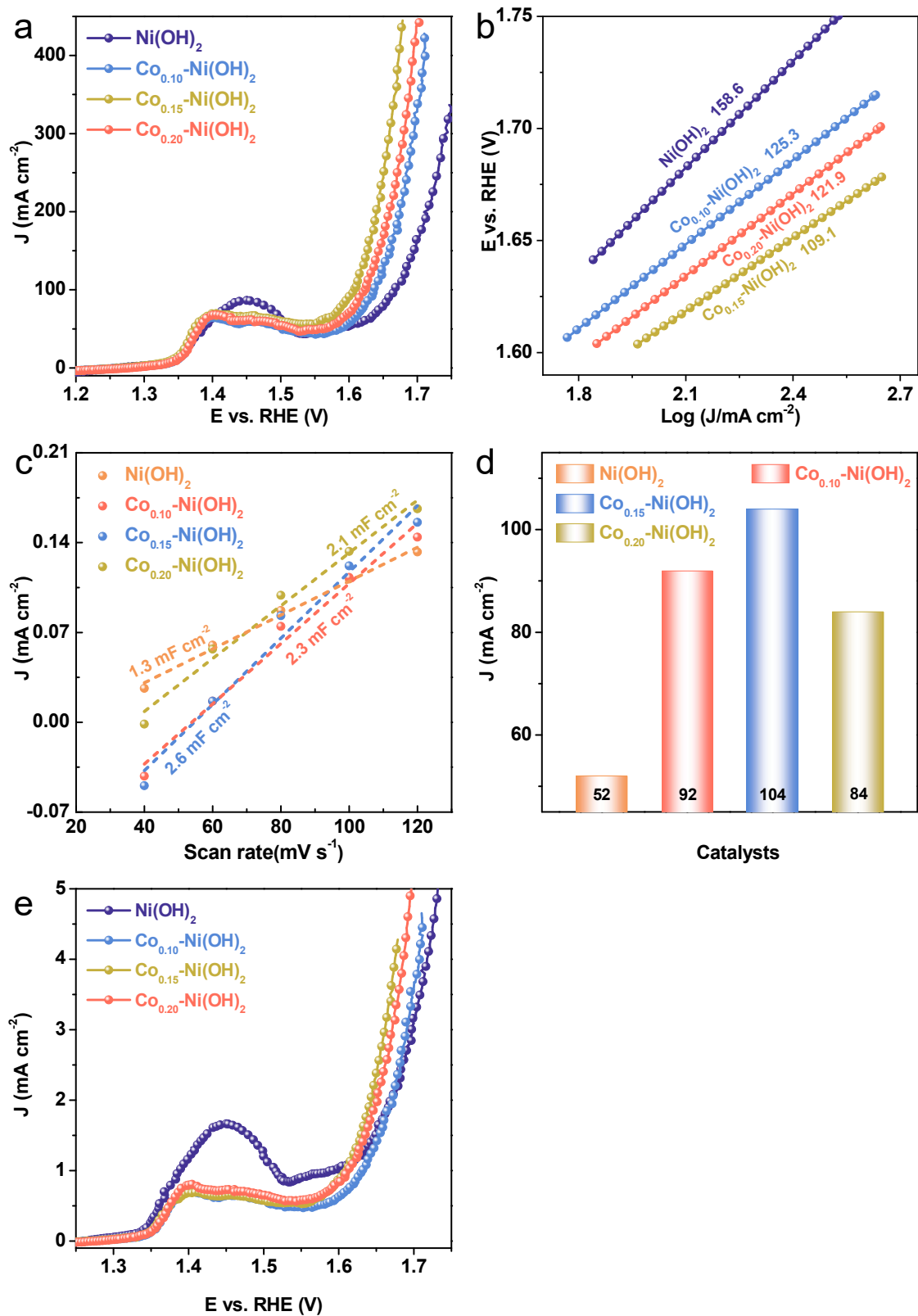


Fig. S24. OER activity of Ni(OH)<sub>2</sub> and Co-doped Ni(OH)<sub>2</sub>. (a) LSV, (b) Tafel slopes, (c)  $C_{dl}$ ,

(d) ECSA and (e) ECSA-normalized LSV.

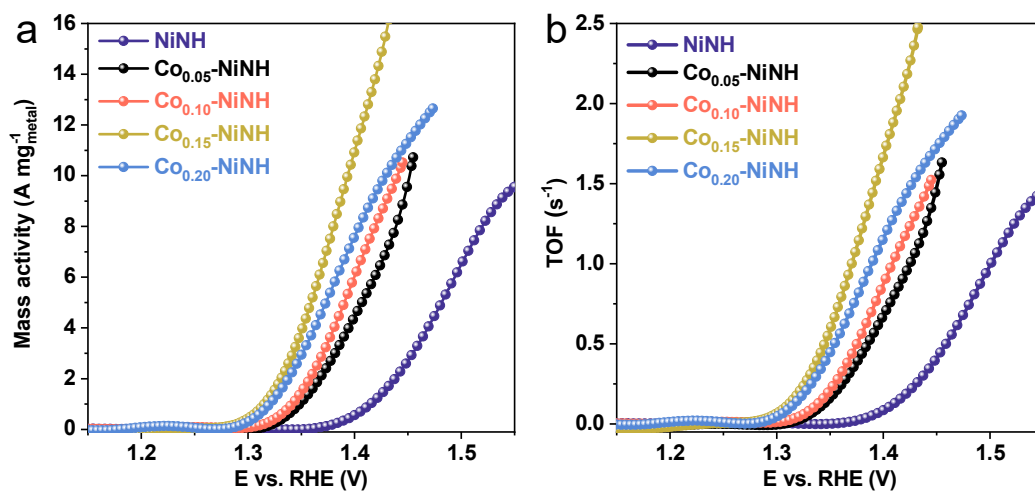
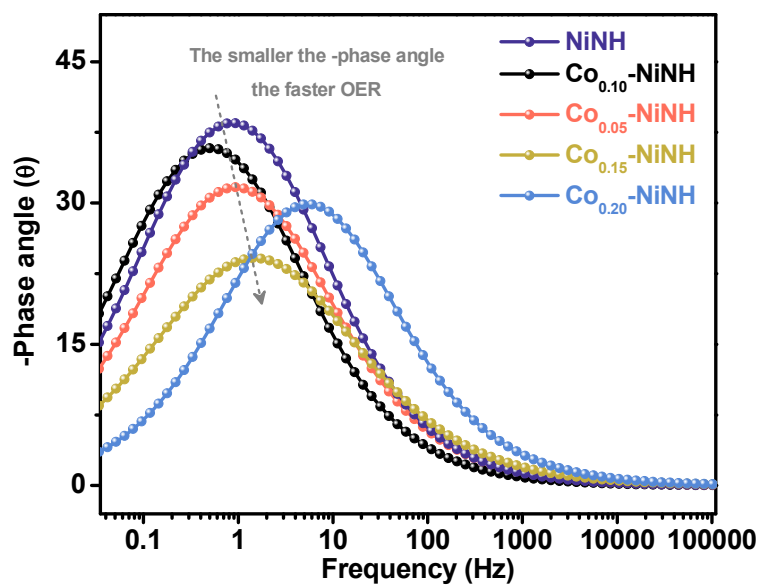


Fig. S25. (a) Mass activities and (b) TOFs of obtained samples.



**Fig. S26.** Bode plots of obtained samples. In our system, OER is a low frequency interfacial reaction. The smaller the -phase angle, the faster OER.

**Table S3.** Element contents of Co and Ni in electrolyte for Co<sub>0.15</sub>-NiNH during 100-h stability

(unit,  $\mu\text{g}\cdot\text{dm}^{-3}$ ).

Element	0 h	25 h	50 h	75 h	100 h
Co	2.01	22.44	23.28	25.45	40.60
Ni	23.11	26.12	32.01	36.65	35.97



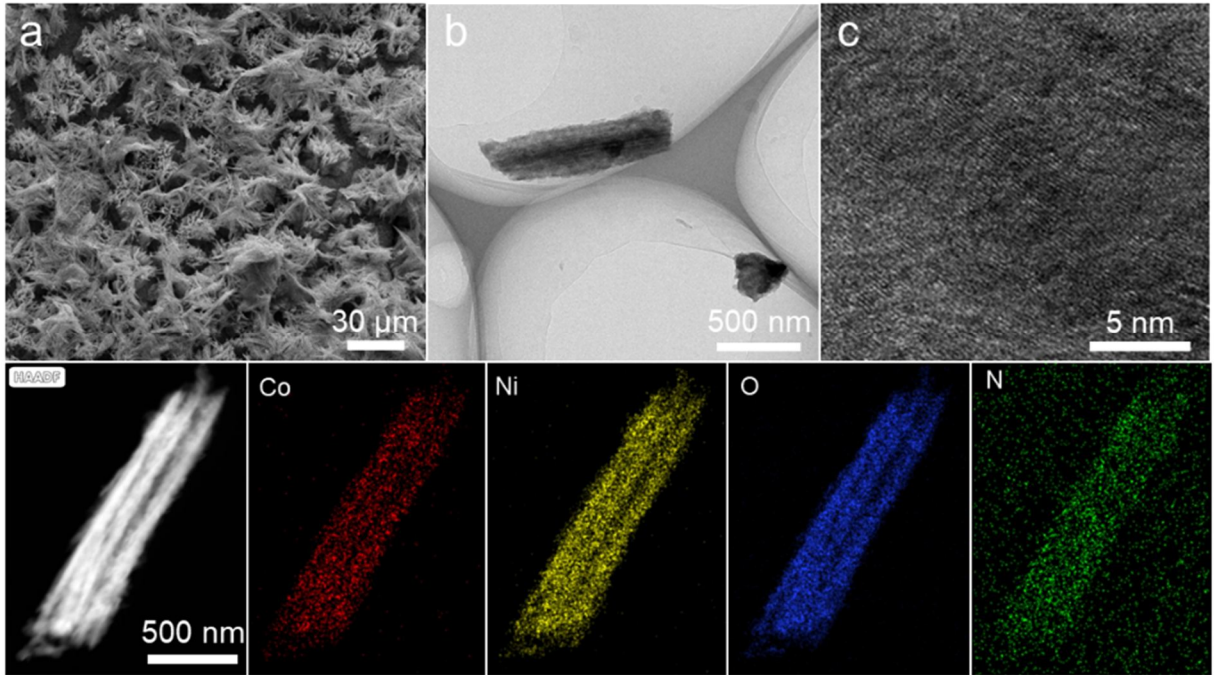


**Fig. S27.** Morphology of  $\text{Co}_{0.15}\text{-NiNH}$  after 100 h-stability test. (a) SEM image, (b) TEM image, (c) HRTEM image. (d) Element mappings of Ni, Co, N and O in  $\text{Co}_{0.15}\text{-NiNH}$ .

**Table S4.** Comparison of alkaline OER performance with previously reported advanced catalysts.

Catalyst	$\eta$ (mV) @100 mA cm <sup>-2</sup>	Tafel slope (mV dec <sup>-1</sup> )	OER activity @ $\eta = 200$ mV		Ref.
			TOF (S <sup>-1</sup> )	Mass activity (A g <sup>-1</sup> )	
Co <sub>0.15</sub> -NiNH	115.8	30.5	2.40	15770	This work
V-NiS	220	39	-	-	12
NiS <sub>x</sub> /C <sub>3</sub> N <sub>4</sub>	110	48	-	-	13
Ni <sub>0.8</sub> Fe <sub>0.2</sub> -AHNAs	225	31.8	-	-	14
Fe <sub>0.53</sub> Ni <sub>0.47</sub> WO <sub>4</sub> /NF	200	35	-	-	15
NiCo <sub>2</sub> S <sub>4</sub> /ZnS	240	47	3.1	-	16
KC-MLH/NF-12	230.2	39.8	0.09	-	17
NiSe@CoFe	236	90.3	0.0783 (250 mV)	184.4	18
KNFF <sub>2</sub> @NF	258	43.7	-	-	19
IrCoO <sub>x</sub> ANSs	220	60.5	-	1412	20
Ir SA-Ni <sub>2</sub> P	266	90.1	-	-	21
NiTe/NiS	257	49	0.178 (300 mV)	-	22
(Ni <sub>x</sub> Fe <sub>1-x</sub> ) <sub>2</sub> P	250	59.3	-	-	23
CoFe MLDH	238	31.5	0.68 (300 mV)	-	24
CdRu <sub>2</sub> IrO <sub>x</sub>	250	55.3	0.43 (250 mV)	562.2	25
Mo,Co-NiS/NF-400	117.2	68.9	-	-	26
CoO <sub>x</sub> /RuO <sub>x</sub> -CC	245	61.2	0.04 (170 mV)	20 (220 mV)	27
MFN-MOFs(2:1)/NF	248	55.4	-	-	28
Ni <sub>3</sub> S <sub>2</sub> /Fe-NiP <sub>x</sub> /NF	230	46.5	0.63 (250 mV)	-	29
Fe MOF-Ni <sub>3</sub> S <sub>2</sub> /N	243	57.7	-	-	30
W-NiS <sub>0.5</sub> Se <sub>0.5</sub>	239	41	0.21 (130 mV)	-	31
Fe-Mo-O/NF	224	30.6	0.64 (224 mV)	-	32
Fe-Ni(O)OH	242	48	-	-	33
NiFeOOH	213	57.4	2.38 (270 mV)	-	34
FeNi-P@NCNT/CW	190	60.9	0.068	-	35

nNFCS	220	36.9	-	-	36
<i>d</i> -NiFe-LDH	200	24.9	-	-	37
MoNiFeS <sub>x</sub> @FeNi <sub>3</sub>	237	72.8	0.215	-	38

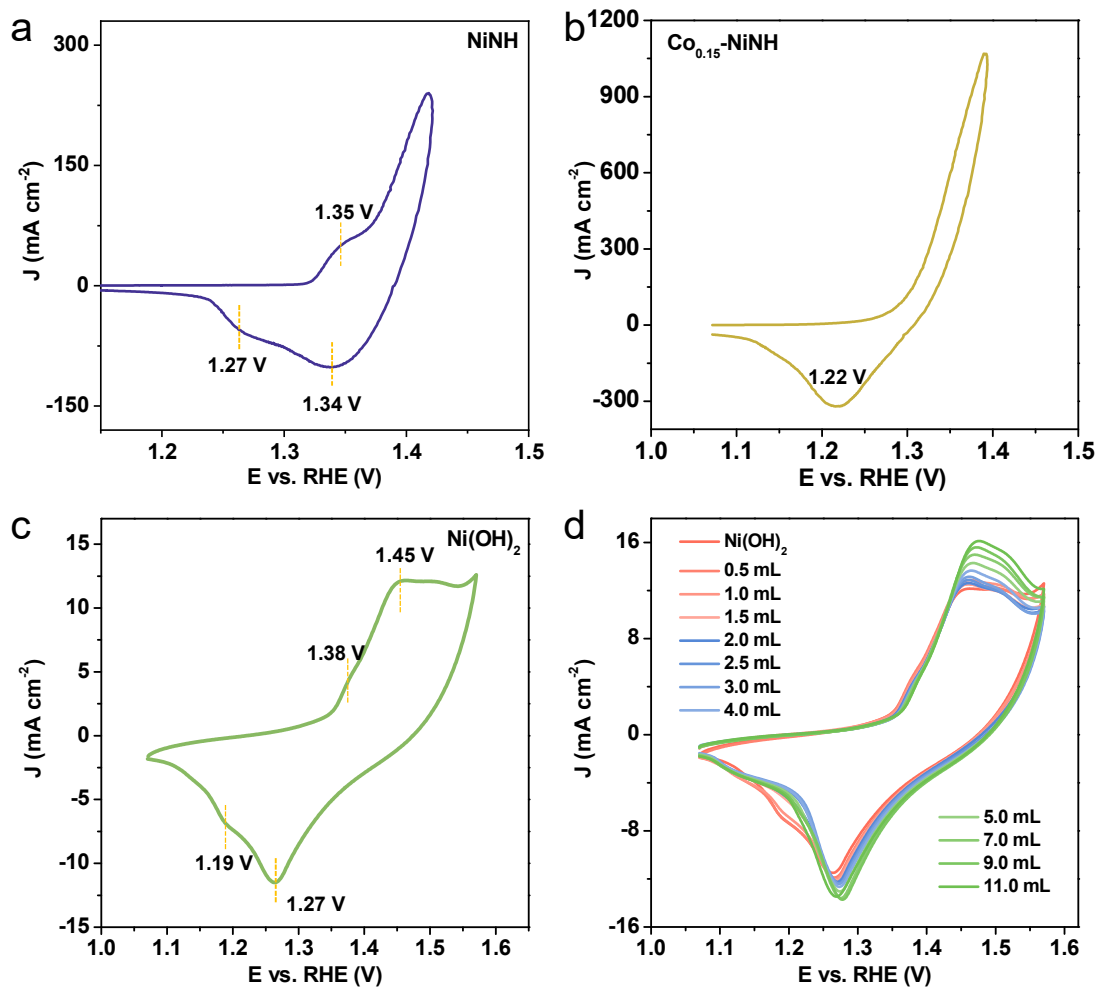


**Fig. S28.** CV curves of (a) NiNH, (b)  $\text{Co}_{0.15}\text{-NiNH}$  and (c)  $\text{Ni(OH)}_2$ . (d) dropping  $\text{KNO}_3$  solution (0.1 M) into electrolyte to observe the changes in the oxidation peak of  $\text{Ni(OH)}_2$ . Compared with the CV curve of  $\text{Ni(OH)}_2$ , the redox peak intensity of NiNH is much higher, indicating that NiNH has efficient oxygen intercalation and deintercalation behavior. NiNH has two consecutive reduction peaks, corresponding to the two electrons transfer from  $\text{Ni}^{4+}$  to  $\text{Ni}^{2+}$ . For  $\text{Ni(OH)}_2$ , 1.38  $\text{V}_{\text{RHE}}$  is the pre-oxidation peak of  $\text{Ni}^{2+}$  to  $\text{Ni}^{3+}$ , while 1.45  $\text{V}_{\text{RHE}}$  is the oxidation peak of  $\text{Ni}^{3+}$  to  $\text{Ni}^{4+}$ . After adding  $\text{KNO}_3$ , the oxidation peak shifts to higher potential, showing that the oxidation the  $\text{Ni}^{3+}$  to  $\text{Ni}^{4+}$  becomes more difficult, which indicates that the existing form of  $\text{NO}_3^-$  in NiNH is different from that of  $\text{NO}_3^-$  in  $\text{Ni(OH)}_2$ .

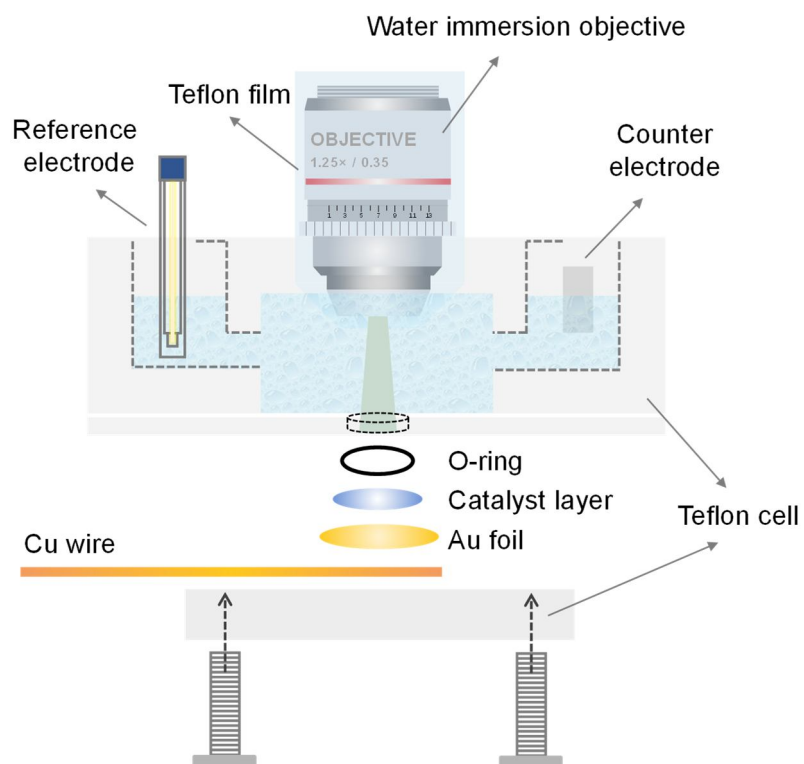


**Fig. S29.** Experimental set-up for the *in-situ* Raman spectroscopy study.

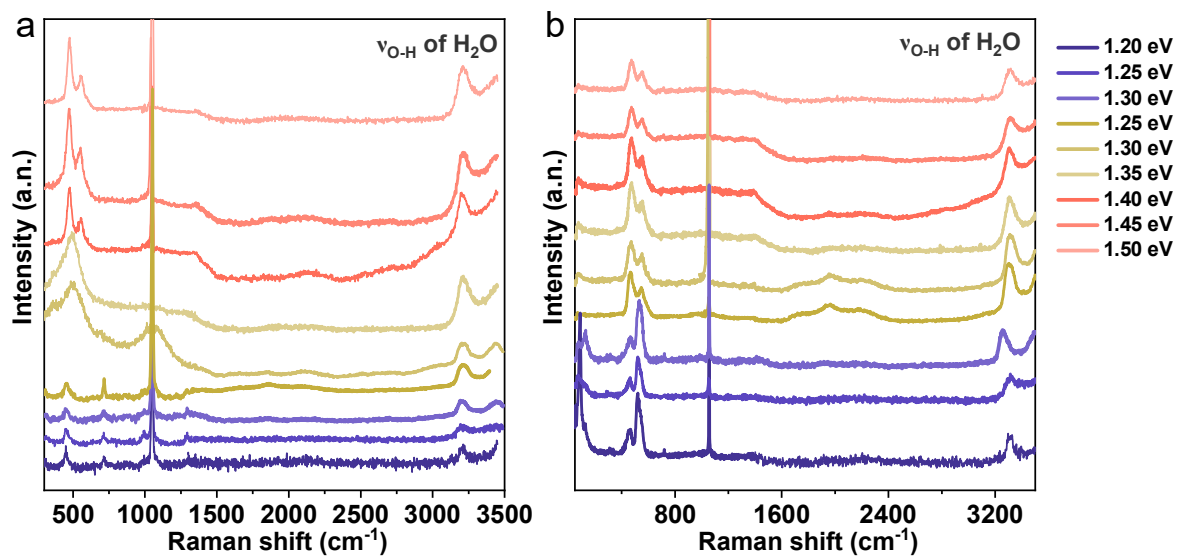


**Fig. S30.** The full-range Raman spectra of (a) NiNH and (b) Co<sub>0.15</sub>-NiNH. The peaks at ~3320 cm<sup>-1</sup> belong to  $\nu_{\text{O-H}}$  of adsorbed H<sub>2</sub>O.

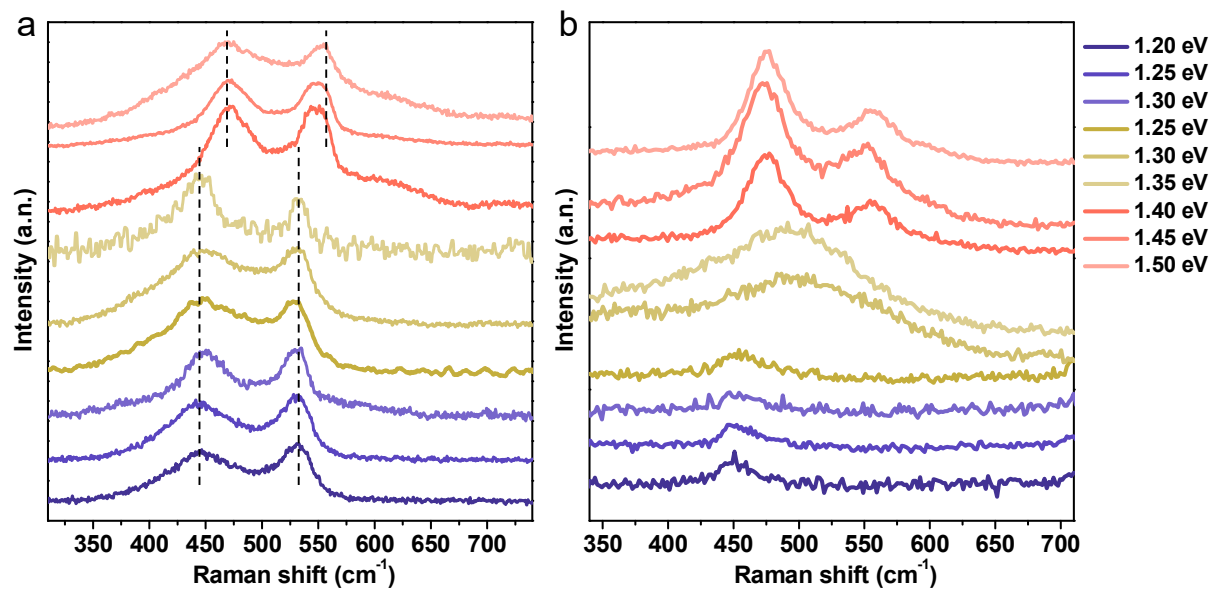


**Fig. S31.** Electrochemical in situ Raman spectra of (a) Ni(OH)<sub>2</sub> and (b) NiNH at the range of 340-710 cm<sup>-1</sup> at the operated potentials from 1.20 to 1.50 V versus RHE.

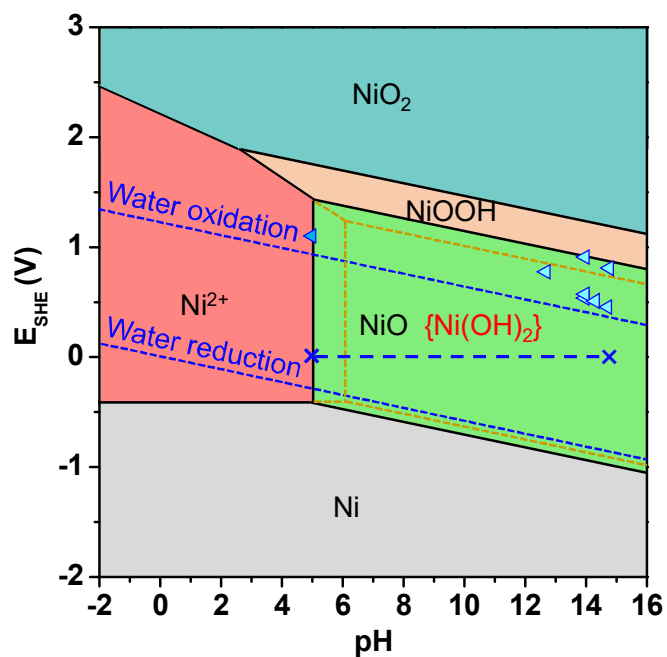


**Fig. S32.** Ni Pourbaix diagrams. The measured oxidation potentials (blue triangles) and stability ranges (cross-capped dotted blue lines) of Ni(OH)<sub>2</sub> and NiO are indicated; The two parallel inclined lines (blue, broken) indicate the potentials for the oxidation ( $2\text{H}_2\text{O} \rightarrow \text{O}_2 + 4\text{H}^+ + 4\text{e}^-$ ) and reduction ( $2\text{H}_2\text{O} + 2\text{e}^- \rightarrow \text{H}_2 + 2\text{OH}^-$ ) of water. The phase domain for the metastable Ni(OH)<sub>2</sub> is also indicated by red dashed lines.



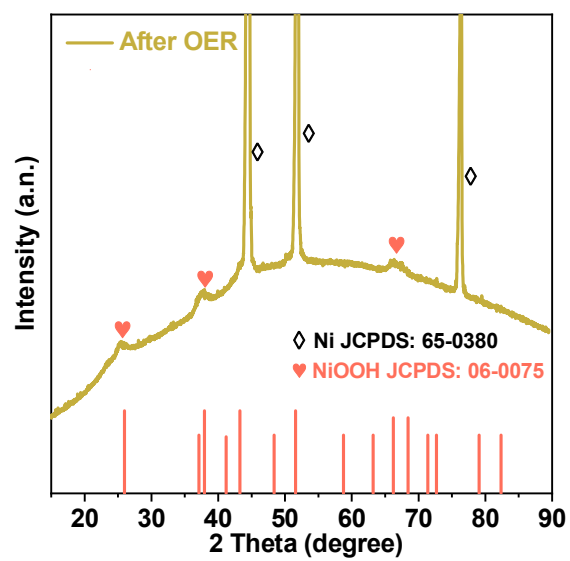


**Fig. S33.** XRD of  $\text{Co}_{0.15}\text{-NiNH}$  after 100 h-stability test.

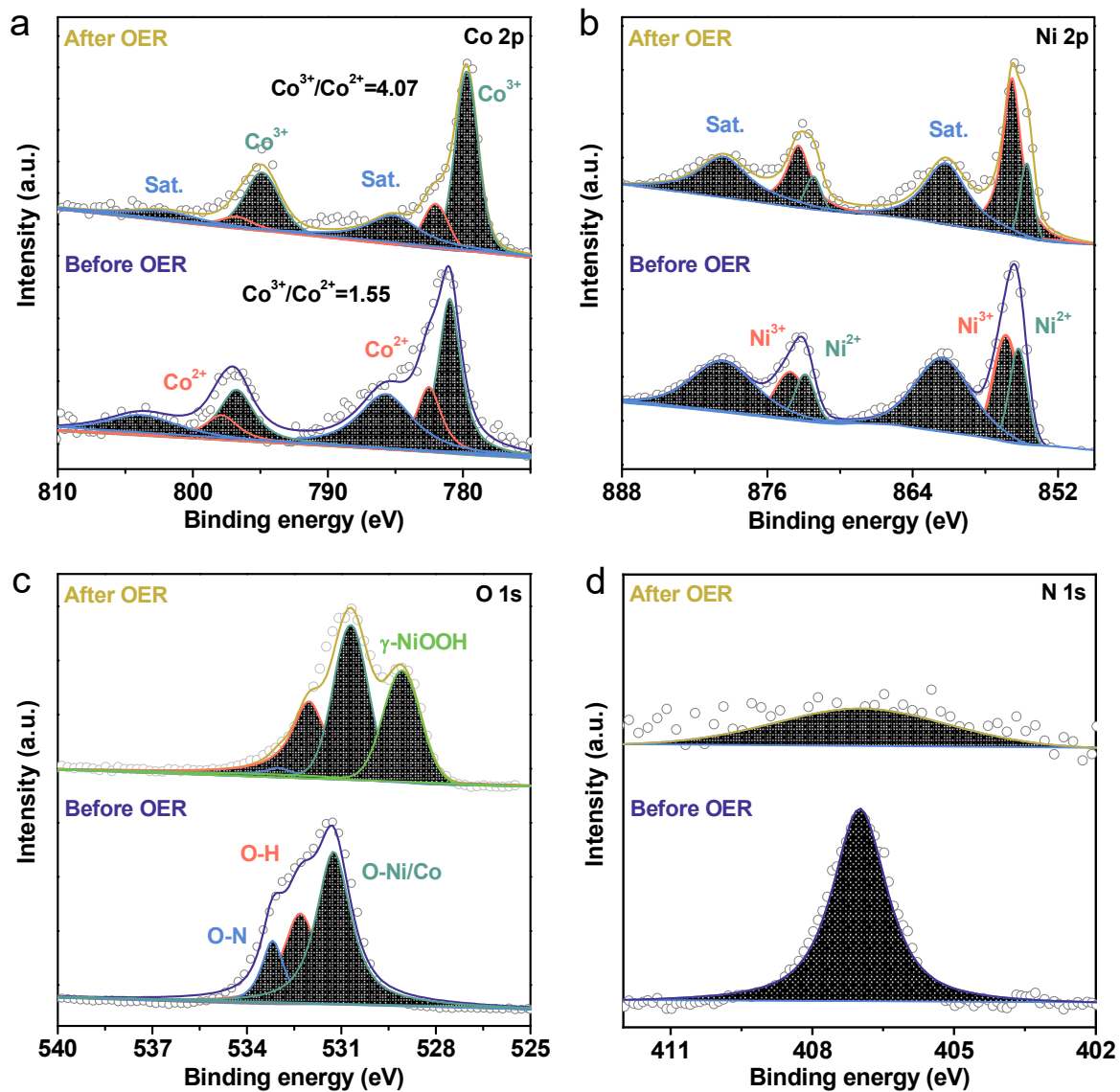
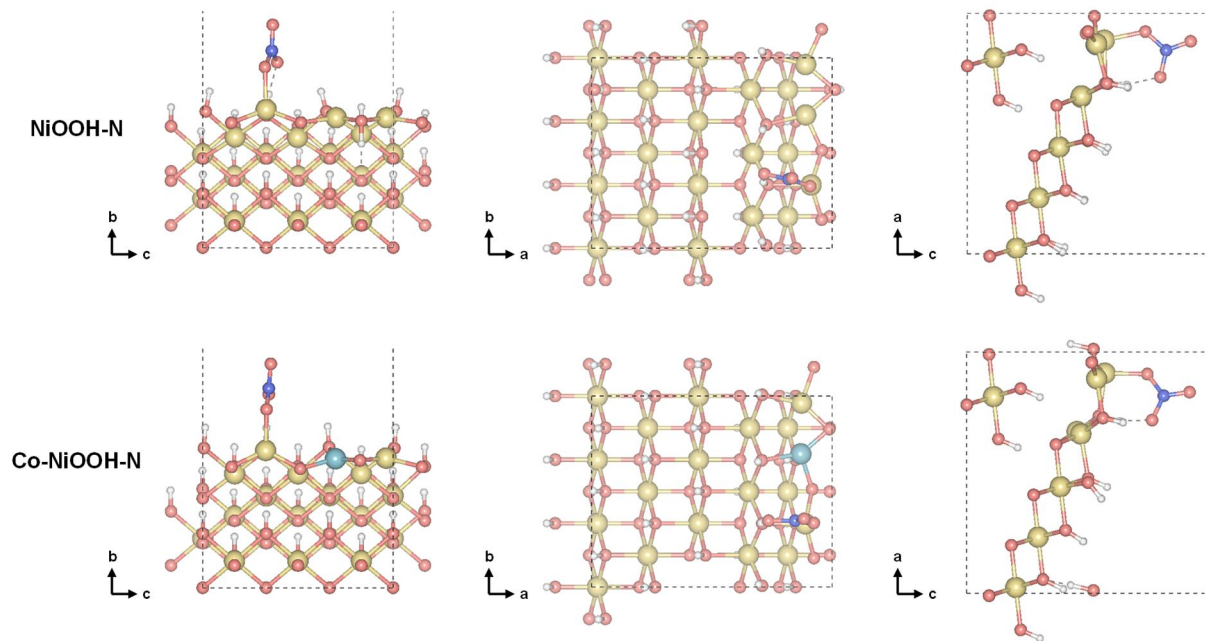
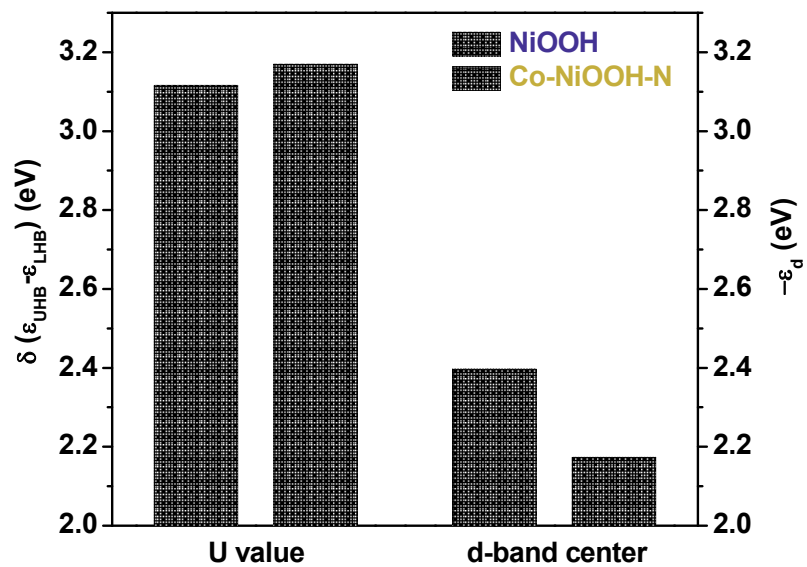


Fig. S34. XPS of  $\text{Co}_{0.15}\text{-NiNH}$  after 100 h-stability test. (a) Co 2p, (b) Ni 2p, (c) O 2p and (d)

N 1s.



**Fig. S35.** Constructed  $\text{NO}_3^-$ -adsorbed NiOOH (NiOOH-N) and Co doped NiOOH-N (Co-NiOOH-N) models. Red ball, O; Yellow, Ni; Blue, Co, purple, N; White, H.



**Fig. S36.** The determined U and d-band center of Ni sites for NiOOH and Co-NiOOH-N models.

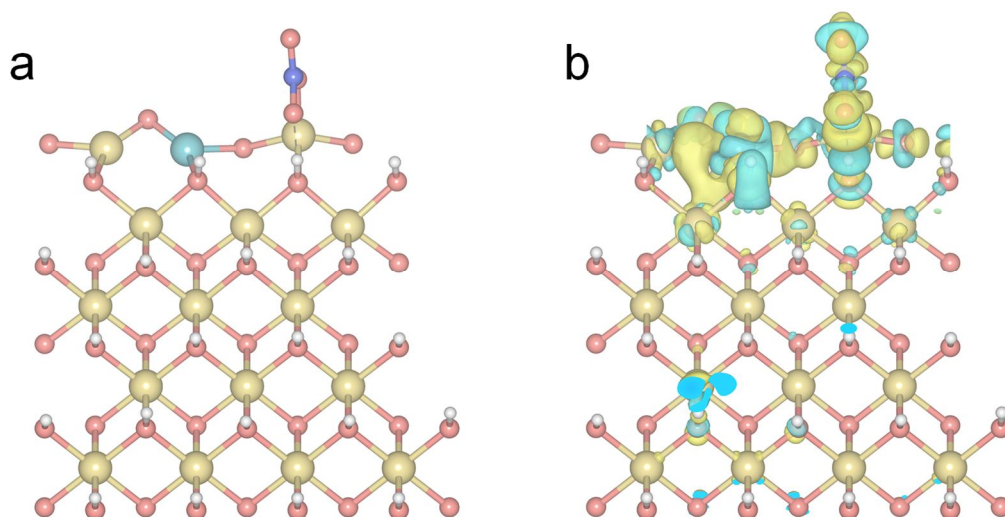


**Fig. S37.** Electron density difference of Co-NiOOH-N model. The yellow color represents electron density increase and the cyan represents electron density decrease. Co and NO<sub>3</sub><sup>-</sup> decreased the electron density of Ni.

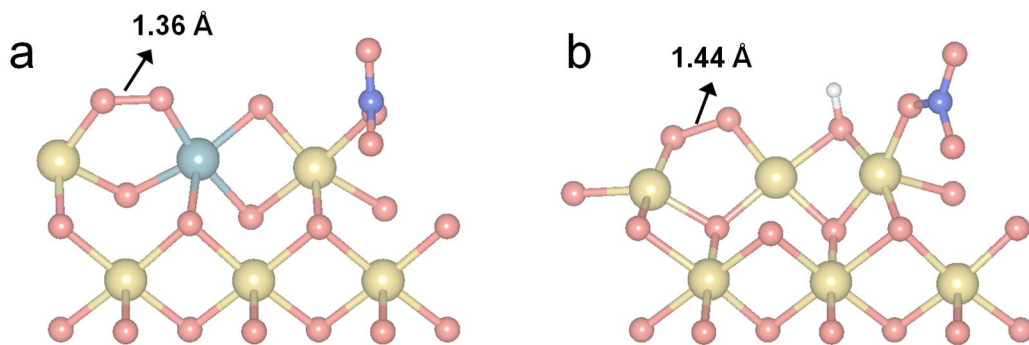


**Fig. S38.** The calculated O-O bond length of lattice oxygen coupled peroxo-like oxygen species in different models. (a) NiOOH-N model. (b) Co-NiOOH-N model. Red ball, O; Yellow, Ni; Blue, Co, purple, N; White, H.

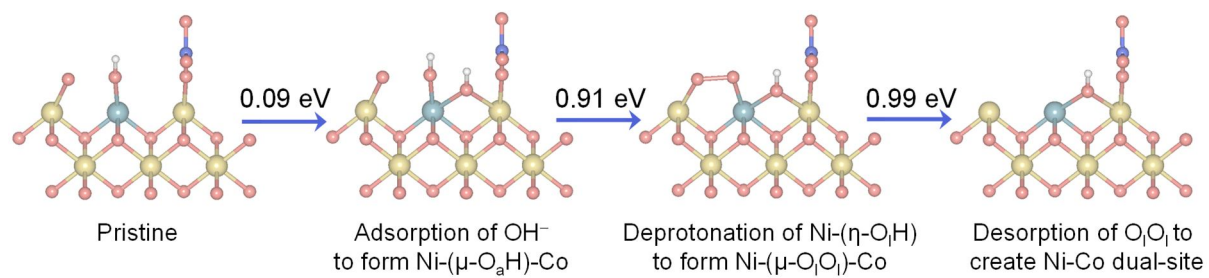


**Fig. S39.** The configuration illustrations of initial evolution of surface oxygen species for

constructing Ni-Co dual-site on Co-NiOOH-N model.

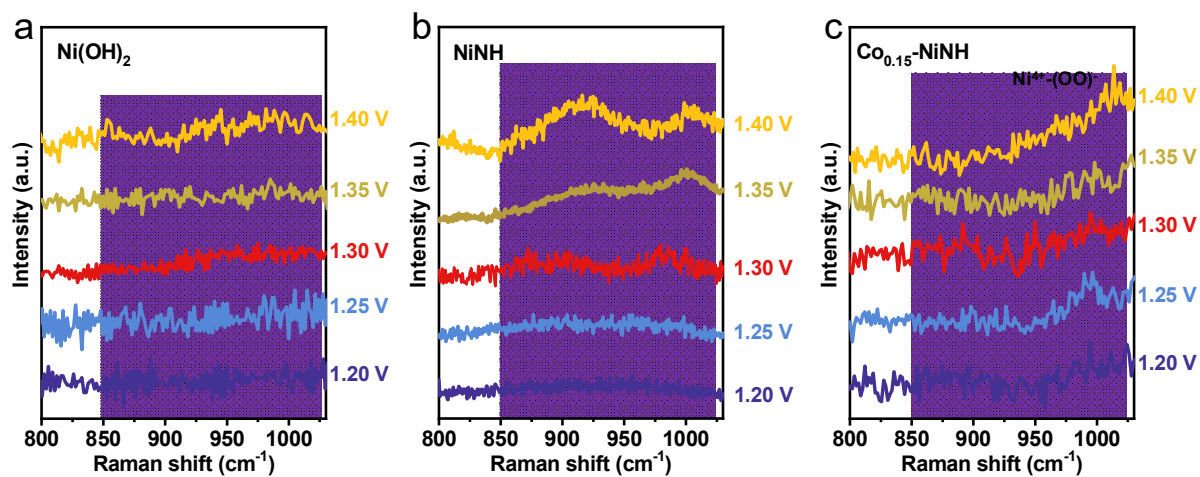


**Fig. S40.** Electrochemical in situ Raman spectra of various catalysts. (a)  $\text{Ni(OH)}_2$ , (b)  $\text{NiNH}$  and (c)  $\text{Co}_{0.15}\text{-NiNH}$ .



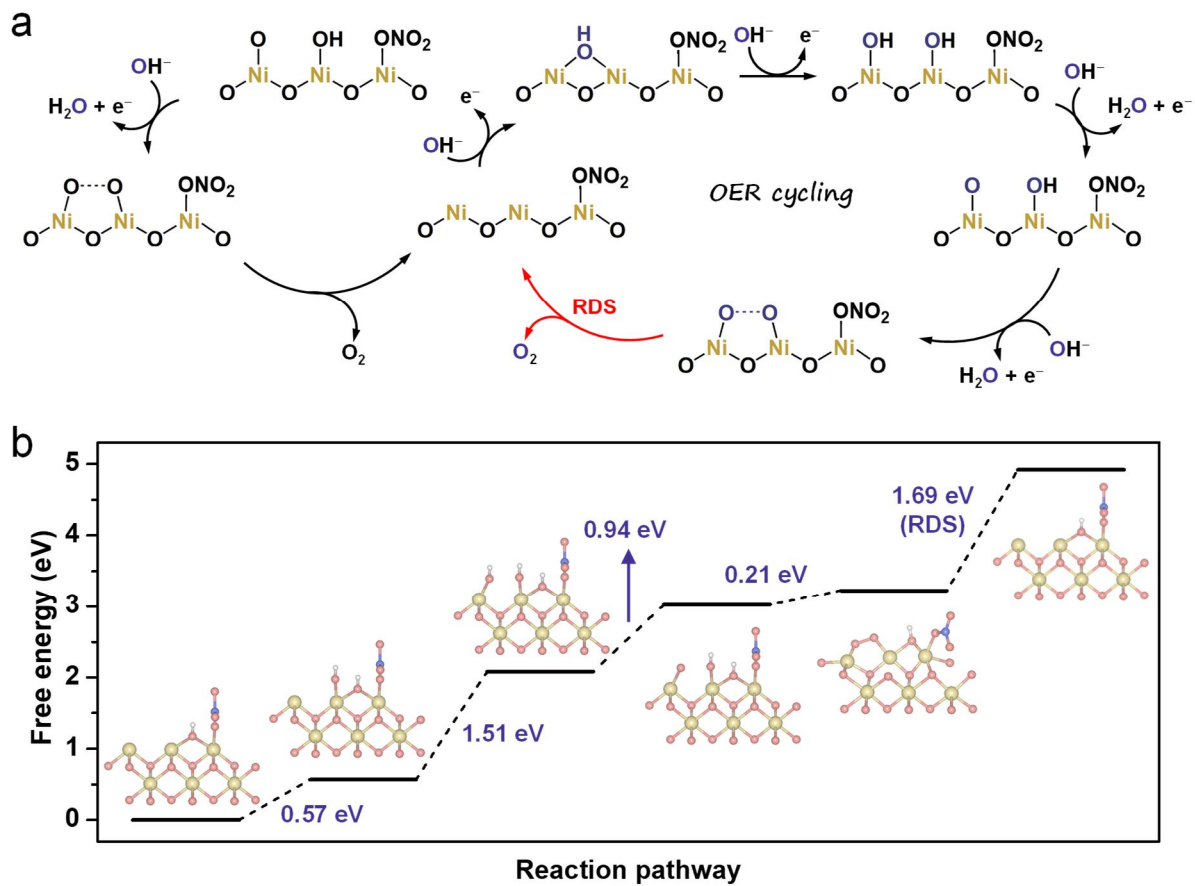


**Fig. S41.** (a) OER cycling on NiOOH-N model. (a) Schematic illustration of the proposed overall OER pathway for NiOOH-N model. (b) The simulated free energy diagrams of OER cycling on NiOOH-N.

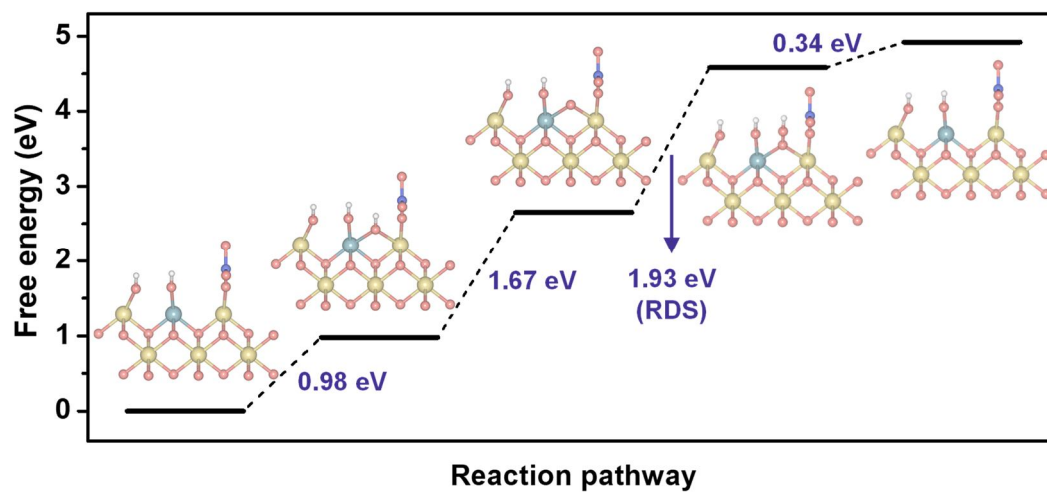


**Fig. S42.** The simulated energy barrier diagram of conventional AEM pathway on Co-NiOOH-N model.

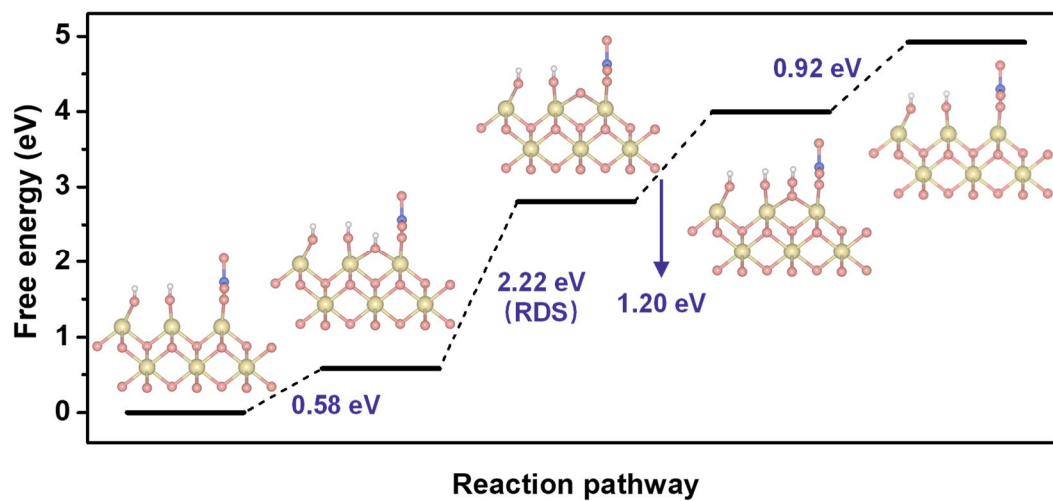


**Fig. S43.** The simulated energy barrier diagram of conventional AEM pathway on NiOOH-N model.

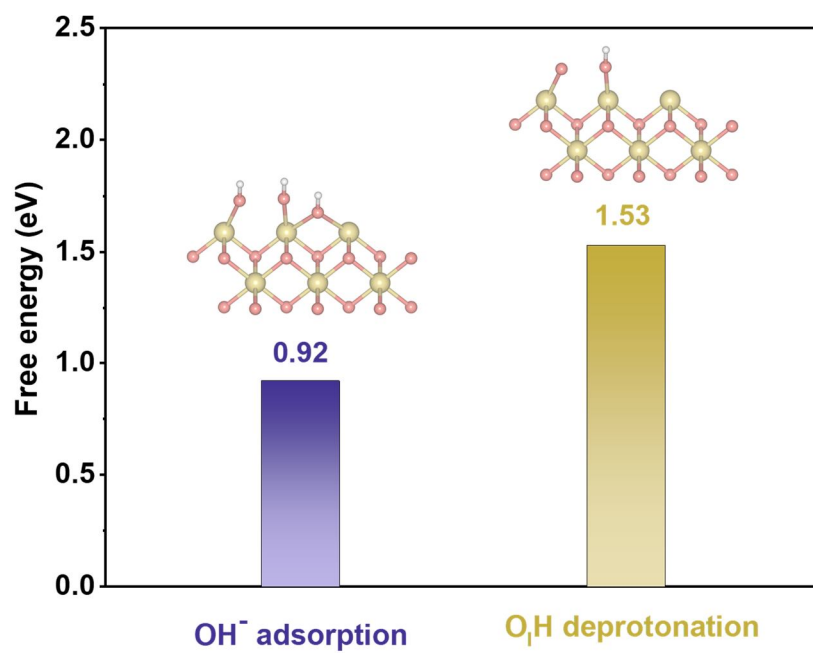


**Fig. S44.** Free energy of OH<sup>-</sup> adsorption and O<sub>1</sub>H deprotonation for NiOOH.

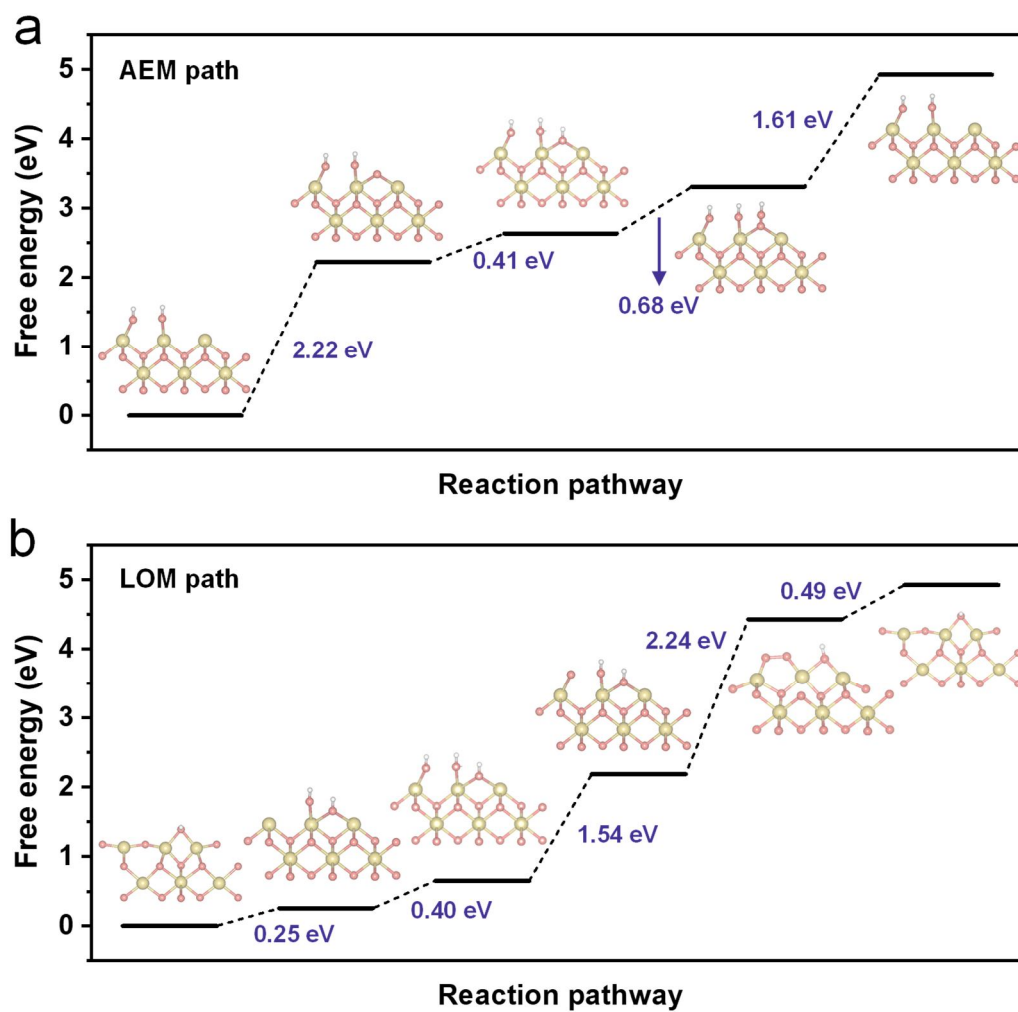
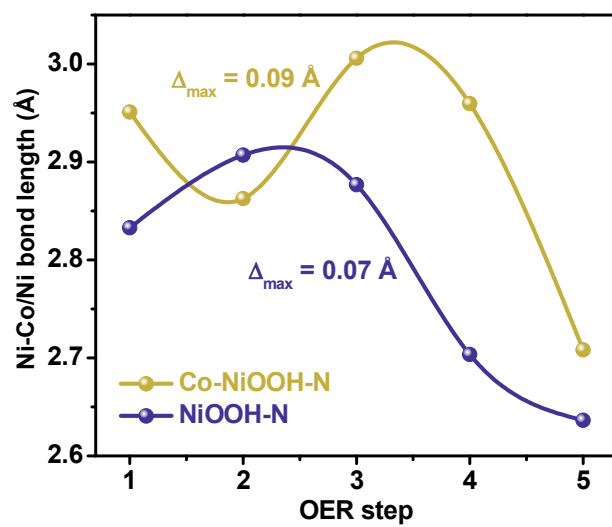
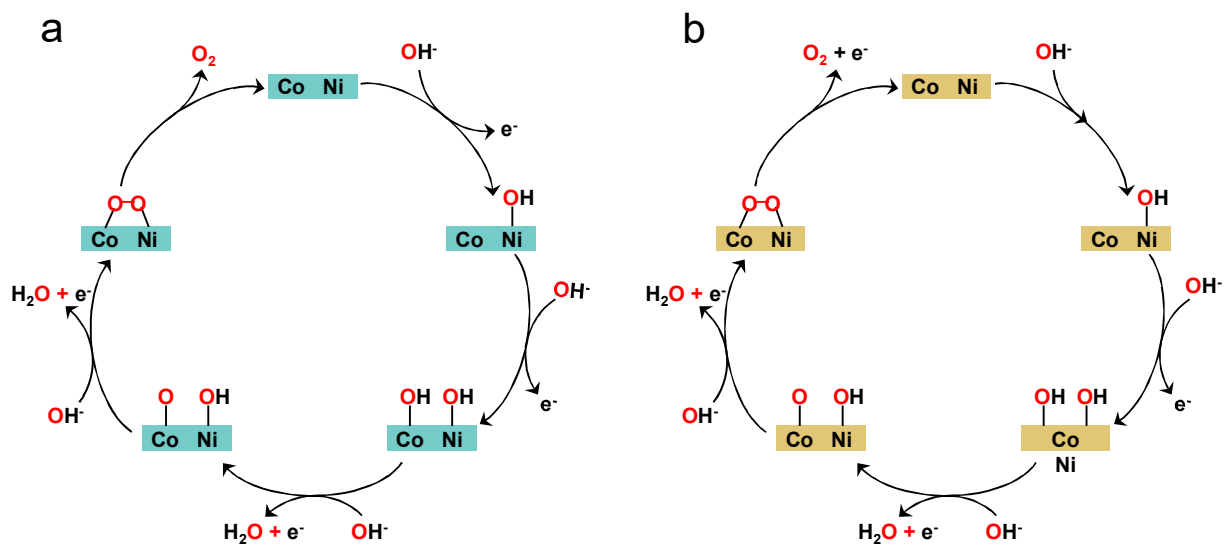


Fig. S45. Gibbs free energy diagram of NiOOH for (a) AEM path and (b) LOM path.



**Fig. S46.** The variation of metal-metal (Ni-Co/Ni) bond length during proposed OER cycling of various models.



**Fig. S47.** Schematic representations of OER cycling on Co-NiOOH-N model. (a) Concerted electron-proton transfer step. (b) Non-concerted electron-proton transfer step.

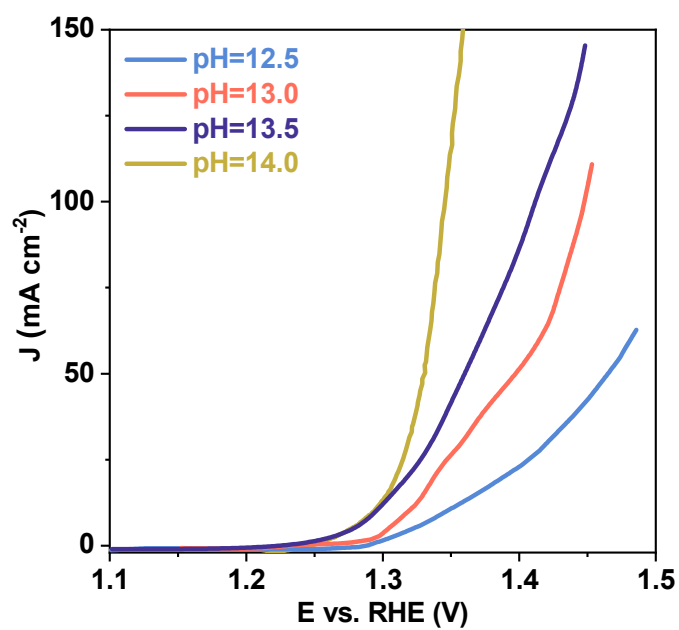


**Fig. S48.** LSV curves of Co<sub>0.15</sub>-NiNH obtained at different pH.



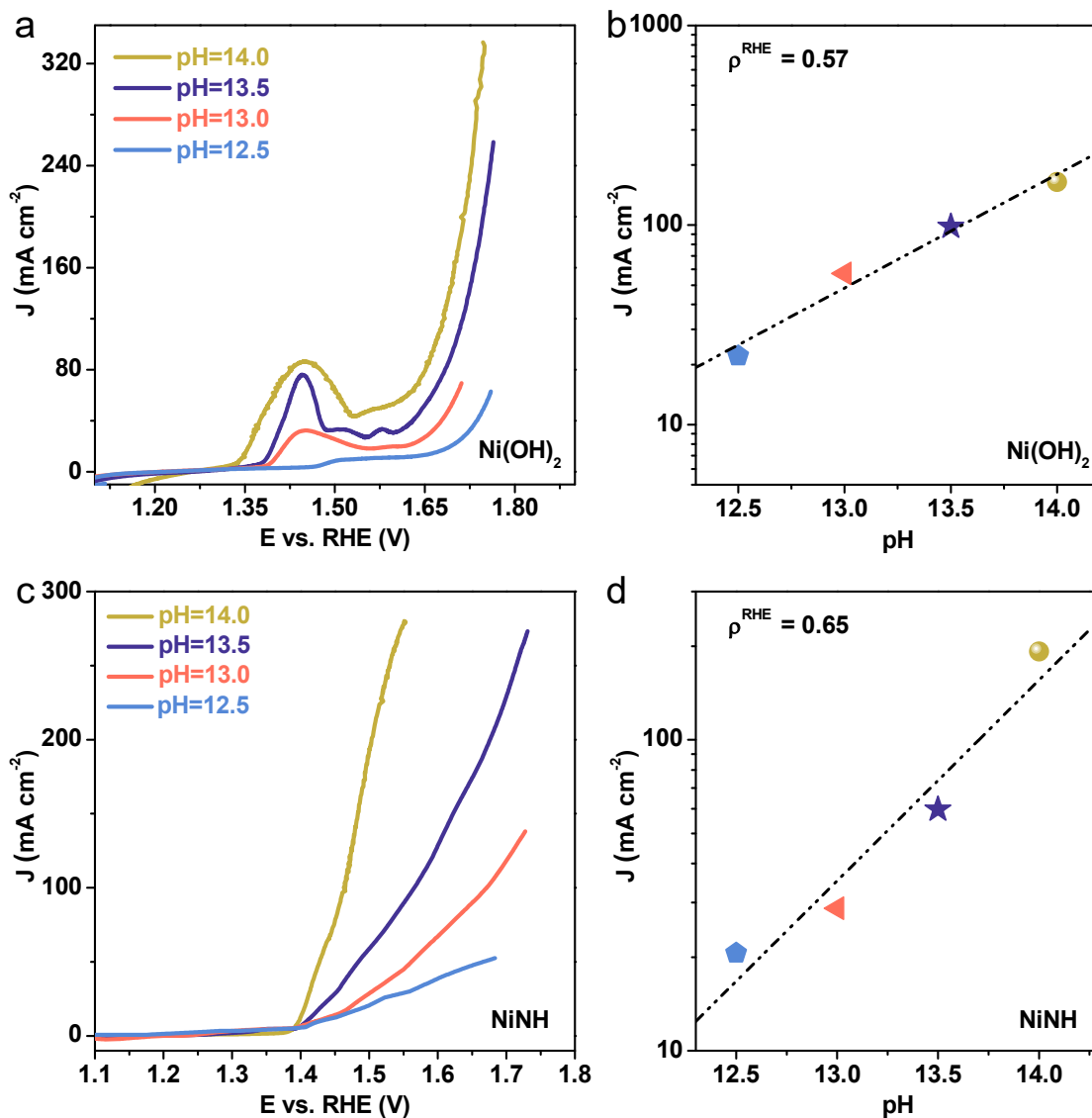


**Fig. S49.** (a) pH dependence of the OER activities of Ni(OH)<sub>2</sub>. (b) Current densities of various catalysts at 1.74 V versus RHE as a function of the pH value. (c) pH dependence of the OER activities of NiNH. (d) Current densities of various catalysts at 1.50 V versus RHE as a function of the pH value.

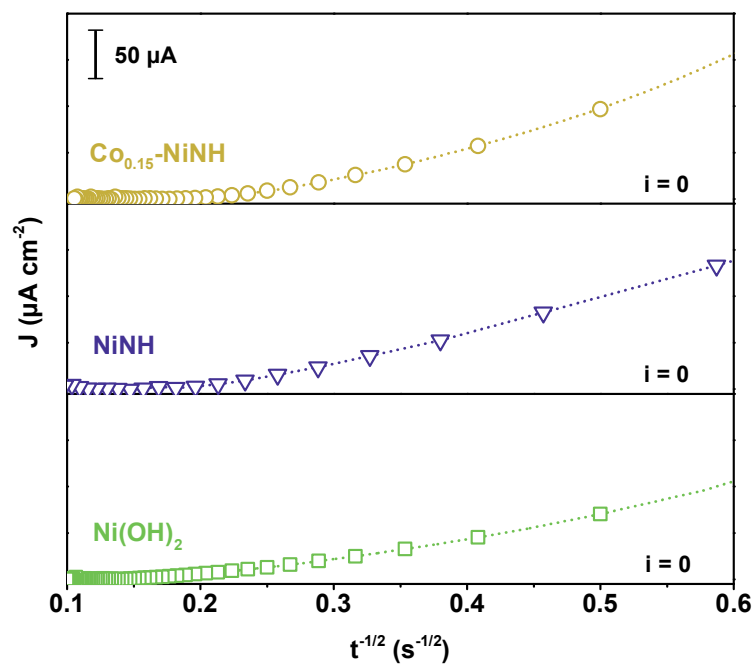


**Fig. S50.** Measured current  $I$  as a function of  $t^{-1/2}$ . The linear portion was fitted to obtain the intercept with the  $t^{-1/2}$  axis (at  $I = 0$ ) for Ni(OH)<sub>2</sub> (0.136), NiNH (0.147) and Co<sub>0.15</sub>-NiNH (0.180).

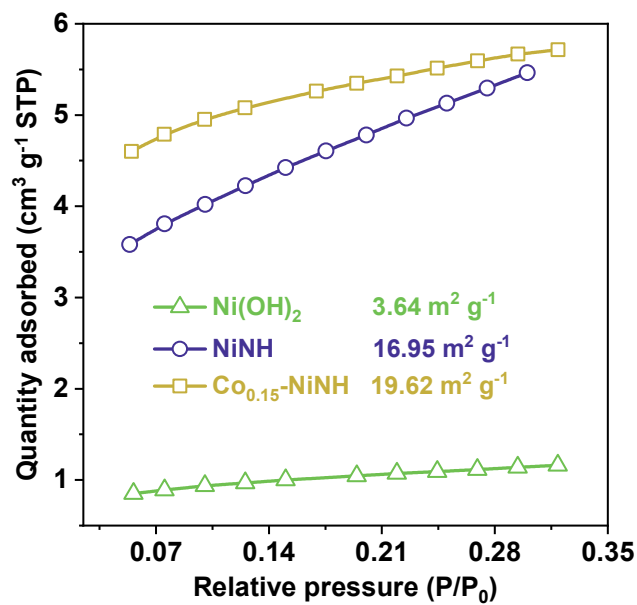
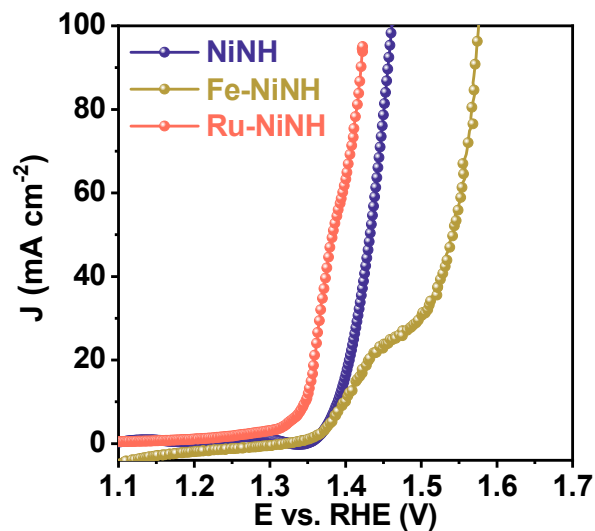


Fig. S51. BET area of  $\text{Ni(OH)}_2$ ,  $\text{NiNH}$  and  $\text{Co}_{0.15}\text{-NiNH}$ .

**Table S5.** Oxygen ion diffusion coefficient (D) of Ni(OH)<sub>2</sub>, NiNH and Co<sub>0.15</sub>-NiNH.

Sample	$\rho$ [g cm <sup>-3</sup> ]	$S_{\text{BET}}$ [m <sup>2</sup> g <sup>-1</sup> ]	a [nm]	$\lambda$	$t^{-1/2}_{(i=0)}$ [s <sup>-1/2</sup> ]	D [ $\times 10^{-12}$ cm <sup>2</sup> s <sup>-1</sup> ]
Ni(OH) <sub>2</sub>	2.4659	3.64	334	2	0.136	5.16
NiNH	0.4316	16.95	410	2	0.147	9.08
Co <sub>0.15</sub> - NiNH	0.4631	19.62	330	2	0.180	8.82



**Fig. S52.** LSV plots of NiNH, Fe-NiNH and Ru-NiNH. It has been reported that Fe(III) can weaken the double exchange effect of the system, while the Ru-Ni system has a moderate double exchange effect, which is related to the reduced OER performance of Fe-NiNH and the enhanced OER performance of Ru-NiNH. Combined with the discussion in this work, the double exchange effect is essential for the OER activity of NiNH<sup>70</sup>.

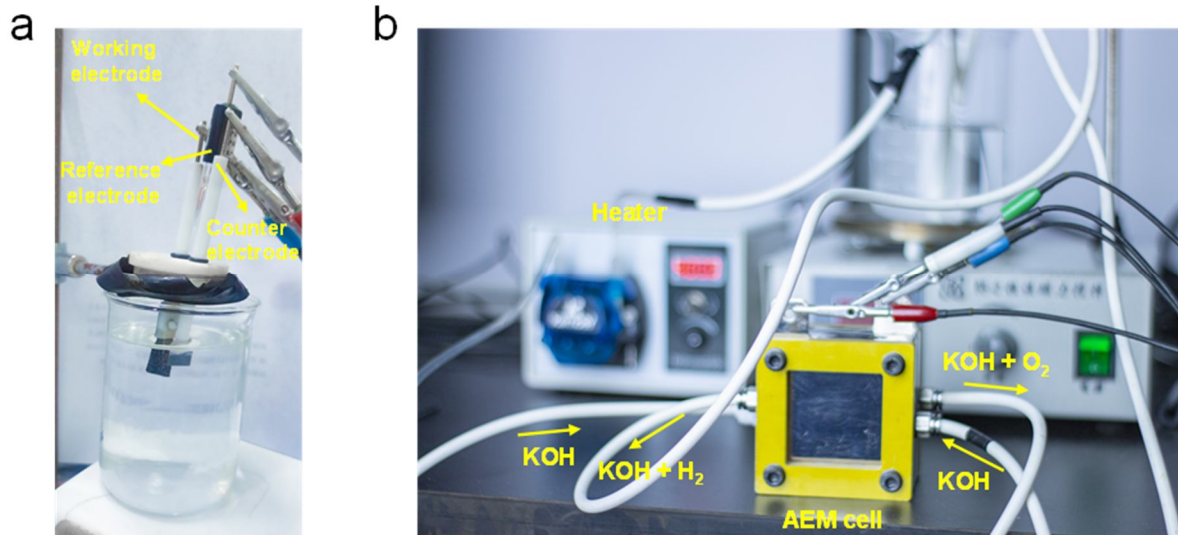


**Fig. S53.** Experimental setup image for three-electrode system and electrolyser.

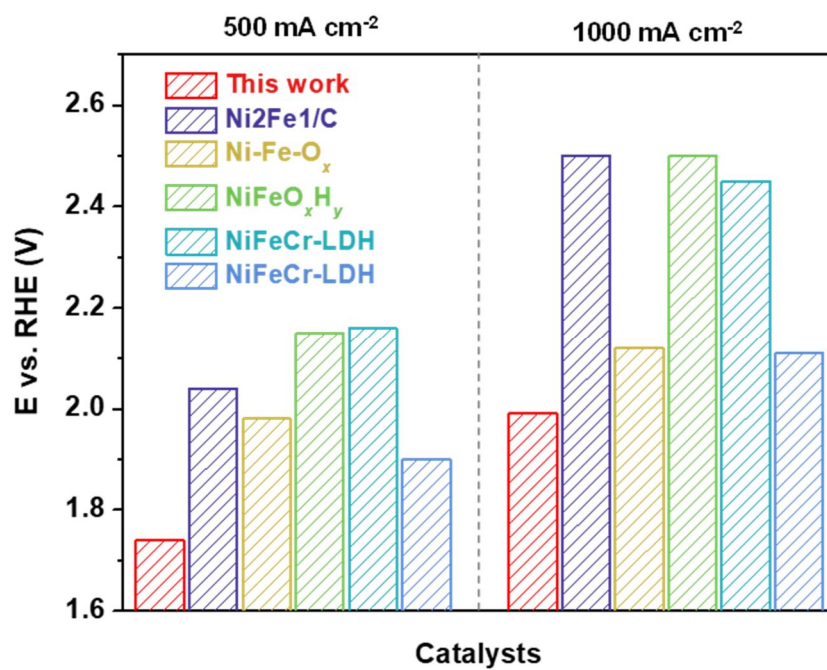


**Fig. S54.** Performance comparison of the single-cell anion exchange membrane water electrolyzer between this work and other reported samples from [Table S6](#). Potentials required at current density of 500 (Left part) and 1000 mA cm<sup>-2</sup> (Right part).

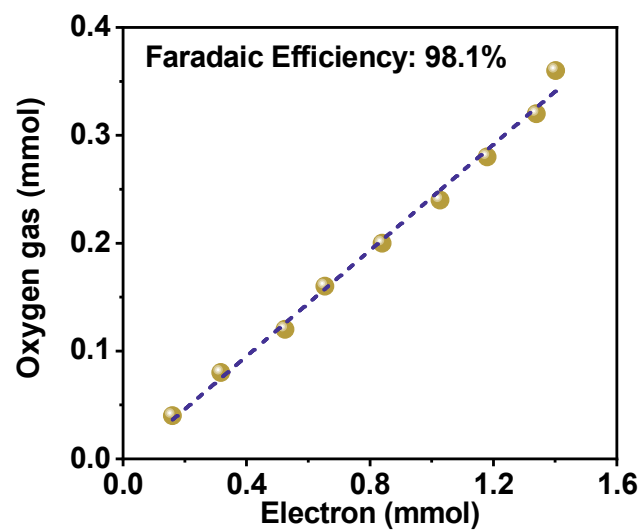


**Fig. S55.** Comparison of evolved O<sub>2</sub> vs. the amount of consumed electrons during the course of electrolysis.



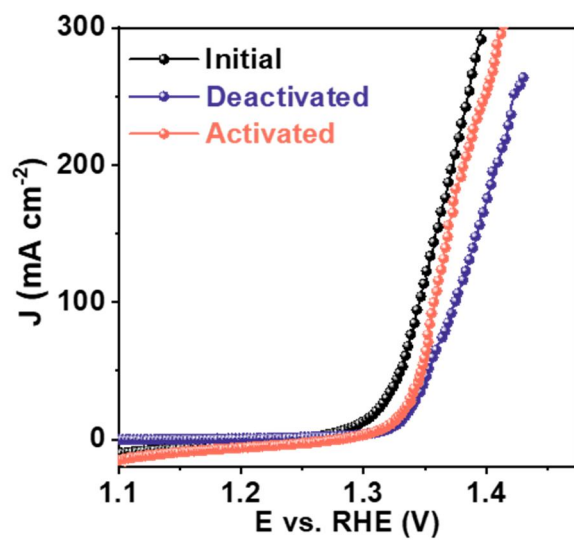


**Fig. S56.** The recyclability test of Co<sub>0.15</sub>-NiNH. A potential of 1.15 V<sub>RHE</sub> was applied to the deactivated Co<sub>0.15</sub>-NiNH sample. Finally, the activity of deactivated Co<sub>0.15</sub>-NiNH (Blue) changes better (Red).

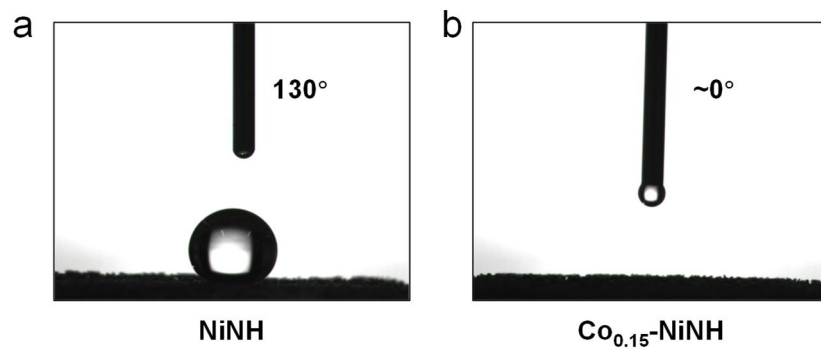


**Fig. S57.** Contact angles of water droplet on the surface of NiNH and Co<sub>0.15</sub>-NiNH.

**Table S6.** Comparison of AEM performance in 1.0 M KOH with previously reported advanced catalysts.

Catalyst	$\eta$ (mV) @500 mA cm <sup>-2</sup>	$\eta$ (mV) @1000 mA cm <sup>-2</sup>	Temperature	Ref.
Co <sub>0.15</sub> -NiNH	1.74	1.99	RT	This work
Ni <sub>2</sub> Fe <sub>1</sub> /C	2.04	2.50	RT	39
Ni-Fe-O <sub>x</sub>	1.98	2.12	RT	40
NiFeO <sub>x</sub> H <sub>y</sub>	2.15	2.50	RT	41
Co(OH) <sub>x</sub> /Ag/Co(OH) <sub>2</sub>	1.63	2.45	50 °C	42
NiFeCr-LDH	2.16	2.45	RT	43
	1.90	2.11	40 °C	
NiFeO <sub>x</sub>	2.00	-	30 °C	44
Cu <sub>x</sub> Mn <sub>0.9-x</sub> Co <sub>2.1</sub> O <sub>4</sub>	> 2.20	-	RT	45
Li <sub>0.21</sub> Co <sub>2.79</sub> O <sub>4</sub>	> 2.20	-	20 °C	46
	> 2.10	-	45 °C	
Fe <sub>2</sub> P <sub>2</sub> S <sub>6</sub> NCs	1.92	> 2.20	50 °C	47

## Supplementary Note 1 | Additional statements for the relationship between electronic structure and OER mechanism.

The orbital interaction and band diagram can be described in Fig. S1a. The overlap of oxygen 2p (O 2p) and metal nd (M nd) orbital induces the bonding (M-O) and antibonding (M-O)\*, dominantly showing oxygen and metal characteristics, respectively<sup>48-50</sup>. The energy difference between (M-O) and (M-O)\* bands is typically defined as charge transfer energy, determined by the electronegativity difference ( $\Delta\chi$ ) between TM and O, which describes the hybridization level of TM nd and O 2p orbitals<sup>48,51</sup>. Further, the electrons in the metal-characterized (M-O)\* antibonding band are further localized by the strong d-d Coulomb interaction (U)<sup>52</sup>. This on-site electron repulsion leads to the (M-O)\* band splitting to the empty upper Hubbard band (UHB) and the electron-filled lower Hubbard band (LHB)<sup>48,52</sup>.

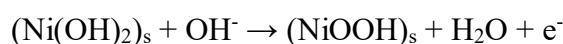
The large electronegativity of oxygen ( $\chi = 3.44$ ) endows materials with strong ionic character of TM-O bond. The O 2p band is deeply aligned in the energy diagram while the TM nd band locates above (Fig. S1b, left). Thermodynamically, cationic redox electrochemistry is more favorable for donating electrons. The electron transfer occurs between the metal center and adsorbed oxygen intermediates to proceed with the OER reaction, following the conventional adsorbate evolution mechanism (AEM) pathway, whilst oxygen ligands will be constrained in the lattice matrix without activation<sup>53,54</sup>. With the decreased charge transfer energy and enlarged U, the electronic band can be manipulated to enable LHB penetrate into the O 2p band (Fig. S1b, middle)<sup>48,55,56</sup>. Thus, intramolecular electron transfer from oxygen ligands to TM cations in the lattice matrix is feasible, leaving ligand holes for lattice oxygen activation, providing the prerequisite for lattice oxygen redox chemistry. To allow the lattice

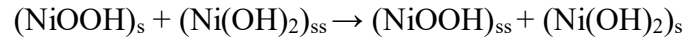
oxygen to participate in oxygen evolution (LOM), the absolute energy level of the O 2p band also needs to be modulated, compared to redox of O<sub>2</sub>/H<sub>2</sub>O ([Fig. S1b, right](#)).

## Supplementary Note 2 | Additional statements for the proton diffusion in Ni(OH)<sub>2</sub>/NiOOH.

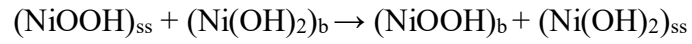
As displayed in Fig. S3, the process of nickel hydroxide oxidation to Ni<sup>4+</sup> is essentially the diffusion transfer of protons (H<sup>+</sup>) through the lattice of Ni(OH)<sub>2</sub> and NiOOH. Lukovstev and Slaiden<sup>57</sup> first put forward the concept of proton diffusion in order to explain the charging and discharging phenomenon of nickel hydroxide electrode. They found that Ni(OH)<sub>2</sub> is a good proton conductor, but not conductive. During the oxidation of β-Ni(OH)<sub>2</sub> to β-NiOOH, OH<sup>-</sup> transfer occurs in the crystal X plane, resulting in the formation of defects in the crystal. These defect vacancies can be occupied by OH<sup>-</sup> in the adsorbed H<sub>2</sub>O state to form hydrogen bonds. In the reduction process, the OH<sup>-</sup> clusters return to the original vacancies. In short, the defect vacancies formed in the lattice of OH<sup>-</sup> and nickel layers can be occupied by hydration molecules (such as LiOH·H<sub>2</sub>O, KOH·H<sub>2</sub>O), and so on.

During anodic oxidation, the activation site on the surface of Ni(OH)<sub>2</sub> particles is oxidized into NiOOH, and protons are released at the same time. Electrons enter the outer circuit through the conductive network. The protons directly react with the OH<sup>-</sup> at the interface on the electrode surface to generate interfacial water. Then, the surface NiOOH reacts with the subsurface Ni(OH)<sub>2</sub>. As a result, the NiOOH is reduced to Ni(OH)<sub>2</sub>, and the Ni(OH)<sub>2</sub> is oxidized to NiOOH, which completes a proton exchange process. Similarly, the subsurface NiOOH reacts with the underlying Ni(OH)<sub>2</sub> to exchange a proton. And so on, protons spread out. There are two ways for protons to diffuse: by hydrogen bonding between Ni(OH)<sub>2</sub> interlayers or by surface diffusion to the active center where they participate in electrochemical reactions. The above electrode reaction mechanism can be expressed as:





...



In the above equation, s represents the surface, b represents the body, and ss represents the subsurface. The first reaction represents the surface electrochemical reaction, corresponding to the charge transfer impedance, while the second represents the bulk diffusion of protons, which is the solid-phase proton diffusion process.

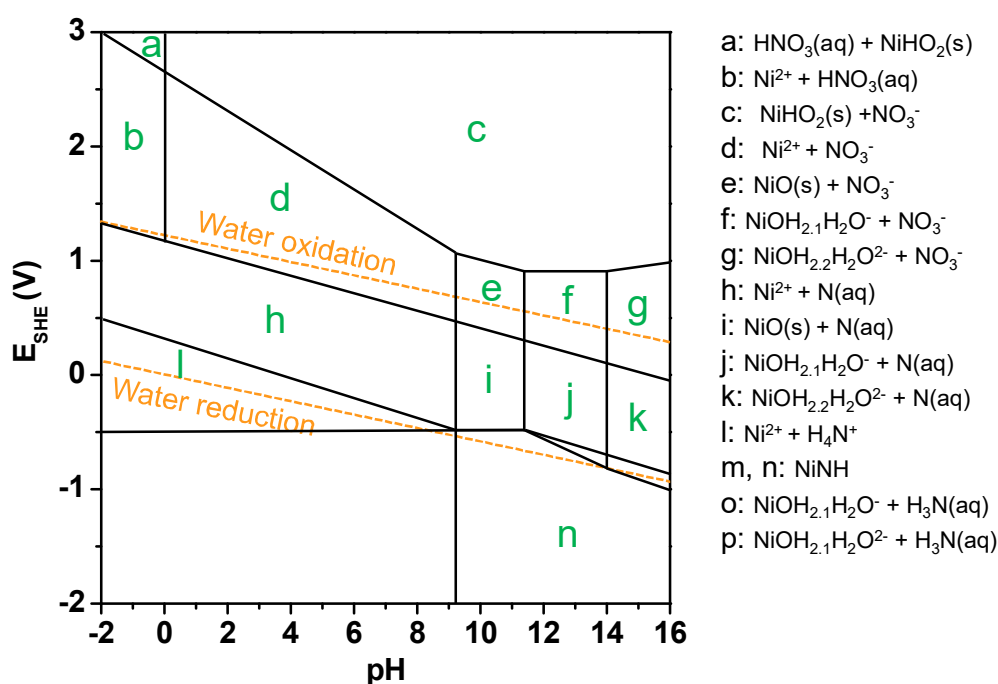
### Supplementary Note 3 | Additional statements for the crystal structure of $\text{Ni}_2(\text{NO}_3)_2(\text{OH})_2 \cdot 2\text{H}_2\text{O}$ .

As illustrated by the stereoscopic view in [Fig. S4](#), antiferromagnetic  $\text{Ni}_2(\text{NO}_3)_2(\text{OH})_2 \cdot 2\text{H}_2\text{O}$  is in the monoclinic P21/c space group ( $a=17.79$ ,  $b=3.15$ ,  $c=14.11$ )<sup>58,59</sup>. The crystal structure of  $\text{Ni}_2(\text{NO}_3)_2(\text{OH})_2 \cdot 2\text{H}_2\text{O}$  is formed by infinite double chains parallel to [010] that share the octahedron  $\text{Ni}_2(\text{NO}_3)_1(\text{OH})_{3/3}(\text{H}_2\text{O})_{2/2}$ . The six-fold coordination of the Ni atom comes from three hydroxide ions, two water molecules and an oxygen atom belonging to the nitrate group. The distances from the two water molecules to the O and O atoms of the nitrate groups are consistent with the criteria valid for hydrogen bonds. The chains are therefore held together by hydrogen bonds from the water molecule to the nitro group at the end of the adjacent chain. [Fig. S4](#) shows the structure projected along different directions. The two different orientations of the double chain exist in a plane perpendicular to the b-axis (the angle between the orientations is about 50°). The corners shared by the three octahedrons in the chain are occupied by hydroxide ions; all the corners shared by the two octahedrons are occupied by water molecules, and the unshared corners at the end are occupied by nitrate oxygen atoms.



**Supplementary Note 4 | Additional statements for the construction of N-Ni(OH)<sub>2</sub> and N-NiOOH.**

On the basis of Ni(OH)<sub>2</sub> and NiOOH structures, we constructed N-Ni(OH)<sub>2</sub> and N-NiOOH. According to the Pourbaix diagram, hydroxynickel nitrate exists as nickel hydroxide and nitrate in an alkaline solution under applied voltage. Therefore, to facilitate the calculations, we made NO<sub>3</sub><sup>-</sup> present in the free form between the layers and expanded the layer spacing by 1 Å.



## Supplementary Note 5 | Additional statements for partial electron transfer (PET) in M-O-M moiety (M = Co and Ni).

As illustrated in Fig. S15, PET can be induced in different metal centers with bridging O<sup>2-</sup> ( $\mu$ -O) through  $\pi$ -donation<sup>60-62</sup>. In this work, considering the  $O_h$  symmetry of hexa-coordinated MO<sub>6</sub>, the valence electronic configuration of Ni<sup>2+</sup>, Co<sup>2+</sup>, Ni<sup>3+</sup>, Co<sup>3+</sup> can be typically determined to be  $3d^8$  ( $t_{2g}^6e_g^2$ ),  $3d^7$  (high-spin (HS),  $t_{2g}^5e_g^2$ )<sup>63</sup>,  $3d^7$  (low-spin (LS),  $t_{2g}^6e_g^1$ )<sup>64</sup> and  $3d^6$  (intermediate-spin (IS),  $t_{2g}^5e_g^1$ ), respectively. Their different electronic configuration of  $3d$ -orbitals (especially for electronic occupancy in  $\pi$ -symmetric  $t_{2g}$ -orbitals) results in distinguished strength of PET. Therefore, Co<sup>3+</sup>-O-Ni<sup>2+</sup>, Co<sup>3+</sup>-O-Ni<sup>3+</sup>, Co<sup>2+</sup>-O-Ni<sup>3+</sup>, Co<sup>2+</sup>-O-Ni<sup>2+</sup> (left metal atom serves as the electron acceptor).

The PET effect can be still effective in highly oxidized states of metal states, as their different electronic configuration of  $3d$ -orbitals. Specially, Ni<sup>4+</sup> and Co<sup>4+</sup> are typically considered to own the electronic configuration of  $3d^6$  (LS,  $t_{2g}^6e_g^0$ ) and  $3d^5$  (IS,  $t_{2g}^4e_g^1$ )<sup>65</sup>. The valence variations typically alter the occupancy of  $e_g$ -orbitals rather than  $\pi$ -symmetric  $t_{2g}$ -orbitals. Hence, electrons can also transfer from Ni<sup>3+/4+</sup> species to Co<sup>4+</sup> species through the proposed PET effect.

## Supplementary Note 6 | Further statements of non-concerted electron-proton transfer step in LOM pathway.

The interdependence of proton and electron transfer has led to a wealth of reaction mechanisms, including those in which electrons and protons occur in steps (ETPT, in which electrons are transferred before protons, or PTET, in which protons are transferred after electrons), and the reaction mechanism of Concerted Proton-Electron Transfer (CPET or CEPT) through a cooperative pathway. Generally, OER proceeds with the concerted electron-proton transfer step, in which the energy barriers of these steps are independent of the proton concentration in the electrolyte, as [Fig. S44](#) displays. It has been well established that the LOM mechanism is concerned with the non-concerted electron-proton transfer step<sup>66,67</sup>. This phenomenon originates from the mismatch between the hydroxide affinity and hydroxide affinity on the interface of electrolyte/catalysts. The  $\text{Ni}^{4+}$  d-band falls below the  $\text{O}_2/\text{H}_2\text{O}$  redox couple to raise the chemical potential of the electron, ultimately lowering or even eliminating the barrier of electron transfer. As a consequence, the electron-proton transfer in water oxidation is decoupled, delivering a pH-correlated OER activity, as shown in [Fig. S44](#).

## Supplementary Note 7 | Oxygen ion diffusivity measurements

The oxygen ion diffusivity measurements were performed in Ar-saturated 1 M KOH solution using CV and chronoamperometry methods<sup>68-70</sup>. In a typical procedure, cyclic voltammetry was performed at 10 mV s<sup>-1</sup> for two cycles. Then the electrode was tested chronoamperometrically by applying a potential 50 mV more than the start potential according to the second CV plot for 4 h. The oxygen ion diffusion coefficient ( $D$ ) was calculated according to the equation  $\lambda = a(Dt)^{-1/2}$  based on a bounded 3D diffusion model. Where  $\lambda$  is a dimensionless shape factor,  $a$  is the radius of the particle. The current was plotted versus  $t^{-1/2}$  and the linear section of the curves was fit to get the intercept with the axis. In this case, we assume that  $\lambda$  is 2 for all the samples, representative of a rounded parallelepiped, halfway between the values for a cube ( $\lambda = 2.26$ ) and a sphere ( $\lambda = 1.77$ ). Parameter  $a$  was estimated by the relation of  $S_{\text{BET}} = 6/(2a\rho)$  based on a spherical geometry approximation, where  $S_{\text{BET}}$  is the BET surface area and  $\rho$  is the theoretical density obtained from XRD analysis. Note that ECSA measures the electrochemical activity surface area of materials, while BET measures the surface area of materials. ECSA can be estimated by the BET method and CV method, but there may be side effects and lack of exact specific capacitance. If these factors can be excluded, it is more accurate to choose ECSA. Otherwise, the BET method is preferred. In this work, it is more accurate to choose BET to detect the diffusion coefficient of oxygen ions.

## Reference

- 1 C. Wei, R.R. Rao, J.Y. Peng, B.T. Huang, I.E.L. Stephens, M. Risch, Z.C. Xu and Y. Shao-Horn, *Adv. Mater.*, 2019, **31**, 1806296.
- 2 C.C.L. McCrory, S. Jung, J.C. Peters and T.F. Jaramillo, *J. Am. Chem. Soc.*, 2013, **135**, 16977–16987.
- 3 Y. Wang, Y.Z. Zhao, L. Liu, W.J. Qin, S.J. Liu, J.P. Tu, Y.P. Qin, J.F. Liu, H.Y. Wu, D.Y. Zhang, A.M. Chu, B.R. Jia, X.H. Qu and M.L. Qin, *Adv. Mater.*, 2022, **34**, 2200088.
- 4 G. Kresse and J. Hafner, *Phys. Rev.*, 1994, **B49**, 14251–14269.
- 5 G. Kresse and J. Furthmüller, *Phys. Rev.*, 1996, **B54**, 11169–11186.
- 6 J.P. Perdew, K. Burke, M. Ernzerhof, *Phys. Rev. Lett.*, 1996, **77**, 3865–3868.
- 7 G. Kresse and D. Joubert, *Phys. Rev.*, 1999, **B59**, 1758–1775.
- 8 S. Grimme, J. Antony, S. Ehrlich and H. Krieg, *J. Chem. Phys.*, 2010, **132**, 154104.
- 9 J.K. Nørskov, J. Rossmeisl, A. Logadottir, L. Lindqvist, J.R. Kitchin, T. Bligaard and H. Jónsson, *J. Phys. Chem.*, 2004, **B108**, 17886–1892.
- 10 J. Rossmeisl, A. Logadottir and J.K. Nørskov, *Chem. Phys.*, 2005, **319**, 178–184.
- 11 A.A. Peterson, F. Abild-Pedersen, F. Studt, J. Rossmeisl and J.K. Nørskov, *Energy Environ. Sci.*, 2010, **3**, 1311–1315.
- 12 X.Z. Liu, J.C. Wang, H.X. Liao, J.Y. Chen, S.H. Zhang, L.M. Tan, X.S. Zheng, D.W. Chu, P.F. Tan and J. Pan, *Nano Lett.*, 2023, **23**, 5027–5034.
- 13 Z.N. Zahran, E.A. Mohamed, Y. Tsubonouchi, M. Ishizaki, T. Togashi, M. Kurihara, K. Saito, T. Yui and M. Yagi, *Energy Environ. Sci.*, 2021, **14**, 5358–5365.
- 14 C.W. Liang, P.C. Zou, A. Nairan, Y.Q. Zhang, J.X. Liu, K.W. Liu, S.Y. Hu, F.Y. Kang, H.J. Fan and C. Yang, *Energy Environ. Sci.*, 2020, **13**, 86–95.
- 15 S. Zhao, F. Hu, L.J. Yin, L.L. Li and S.J. Peng, *Sci. Bul.*, 2023, **68**, 1389–1398.
- 16 J. Sun, H. Xue, N.K. Guo, T.S. Song, Y.R. Hao, J.W. Sun, J.W. Zhang and Q. Wang, *Angew.*

- Chem. Int. Ed.*, 2021, **60**, 19435–19441.
- 17 G.M. Mu, G.Z. Wang, Q.P. Huang, Y.J. Miao, D. Wen, D.M. Lin, C.G. Xu, Y.J. Wan, F.Y. Xie, W.H. Guo and R.Q. Zou, *Adv. Funct. Mater.*, 2023, **33**, 2211260.
- 18 F. Nie, Z. Li, X.P. Dai, X.L. Yin, Y.H. Gan, Z.H. Yang, B.Q. Wu, Z.T. Ren, Y.H. Cao and W.Y. Song, *Chem. Eng. J.*, 2022, **431**, 134080.
- 19 J. Zhang, Y. Ye, Z.B. Wang, Y. Xu, L.Q. Gui, B.B. He and L. Zhao, *Adv. Sci.*, 2022, **9**, 2201916.
- 20 C. Cai, M.Y. Wang, S.B. Han, Q. Wang, Q. Zhang, Y.M. Zhu, X.M. Yang, D.J. Wu, X.T. Zu, G.E. Sterbinsky, Z.X. Feng and M. Gu, *ACS Catal.*, 2021, **11**, 1, 123–130.
- 21 Q. Wang, Z. Zhang, C. Cai, M.Y. Wang, Z.L. Zhao, M.H. Li, X. Huang, S.B. Han, H. Zhou, Z.X. Feng, L. Li, J. Li, H. Xu, J.S. Francisco and M. Gu, *J. Am. Chem. Soc.*, 2021, **143**, 13605–13615.
- 22 Z.Q. Xue, X. Li, Q.L. Liu, M.K. Cai, K. Liu, M. Liu, Z.F. Ke, X.L. Liu and G.Q. Li, *Adv. Mater.*, 2019, **31**, 1900430.
- 23 S.F. Sun, X. Zhou, B.W. Cong, W.Z. Hong and G. Chen, *ACS Catal.*, 2020, **10**, 9086–9097.
- 24 L.Y. Hu, R.S. Xiao, X. Wang, X.S. Wang, C.L. Wang, J. Wen, W.L. Gu and C.Z. Zhu, *Appl. Catal. B Environ.*, 2021, **298**, 120599.
- 25 S.H. Liu, H. Tan, Y.C. Huang, Q.B. Zhang, H.P. Lin, L. Li, ZW. Hu, W.H. Huang, C.W. Pao, J.F. Lee, Q.Y. Kong, Q. Shao, Y. Xu and X.Q. Huang, *Adv. Mater.*, 2023, **35**, 2305659.
- 26 C.Y. Wu, Y.M. Du, Y.L. Fu, D. Feng, H. Li, Z.Y. Xiao, Y.R. Liu, Y. Yang and L. Wang, *Sustainable Energy Fuels*, 2020, **4**, 1654–1664.
- 27 L.M. Deng, S.Y. Liu, D. Liu, Y.M. Chang, L.L. Li, C.S. Li, Y. Sun, F. Hu, H.Y. Chen, H. Pan and S.Y. Peng, *Small*, 2023, **19**, 2302238.
- 28 D.S. Raja, H.W. Lin and S.Y. Lu, *Nano Energy*, 2019, **57**, 1–13.
- 29 X. Luo, P.X. Ji, P.Y. Wang, X. Tan, L. Chen and S.C. Mu, *Adv. Sci.*, 2022, **9**, 2104846.

- 30 X.Y. Wang, M. Zhu, Q.N. Bian, B.S. Guo, W.Q. Kong, C.B. Wang and Y.Y. Feng, *ACS Appl. Nano Mater.*, 2023, **6**, 5200–5210.
- 31 Y. Wang, X.P. Li, M.M. Zhang, J.F. Zhang, Z.L. Chen, X.R. Zheng, Z.L. Tian, N.Q. Zhao, X.P. Han, K. Zaghbi, Y.S. Wang, Y.D. Deng and W.B. Hu, *Adv. Mater.*, 2022, **34**, 2107053.
- 32 X.B. Meng, B.B. Yuan, Y.W. Liu, Z.Q. Zhao, K. Li and Y.Q. Lin, *ACS Appl. Nano Mater.*, 2022, **5**, 9427–9434.
- 33 W. Hua, H.H. Sun, M.W. Jiang, L.B. Ren, Y. Zhang and J.G. Wang, *J. Mater. Chem. A*, 2022, **10**, 7366–7372.
- 34 Y.J. Zhang, K. Dastafkan, Q. Zhao, J.P. Li, C. Zhao and G. Liu, *Appl. Catal. B Environ.*, 2024, **341**, 123297.
- 35 X. Tao, H. Xu, S. Luo, Y.Q. Wu, C.H. Tian, X.H. Lu and Y. Qing, *Appl. Catal. B Environ.*, 2020, **279**, 119367.
- 36 X. Yu, W.W. Zhang, L.L. She, Y.Y. Zhu, Y. Fautrelle, Z. Ren, G.H. Cao, X.G. Lu and X. Li, *Chem. Eng. J.*, 2022, **430**, 133073.
- 37 Z. Li, Y.G. Zhou, M.H. Xie, H. Cheng, T. Wang, J. Chen, Y. Lu, Z.L. Tian, Y.Q. Lai and G.H. Yu, *Angew. Chem. Int. Ed.*, 2023, **62**, e202217815.
- 38 Q. Li, W.X. Zhang, J. Shen, X.Y. Zhang, Z. Liu and J.Q. Liu, *J. Alloys Compd.*, 2022, **902**, 163670.
- 39 Y.J. Ko, M.H. Han, H. Kim, J.-Y. Kim, W.H. Lee, J. Kim, J.Y. Kwak, C.H. Kim, T.E. Park, S.H. Yu, W.S. Lee, C.H. Choi, P. Strasser and H.S. Oh, *Chem Catal.*, 2022, **2**, 2312–2327.
- 40 I. Vincent, E.C. Lee and H.M. Kim, *Catalysts*, 2022, **12**, 476.
- 41 D.Y. Xu, M.B. Stevens, M.R. Cosby, S.Z. Oener, A.M. Smith, L.J. Enman, K.E. Ayers, C.B. Capuano, J.N. Renner, N. Danilovic, Y.G. Li, H.Z. Wang, Q.H. Zhang and S.W. Boettcher, *ACS Catal.*, 2019, **9**, 7–15.
- 42 W.W. Guo, J. Kim, H. Kim, G.H. Han, H.W. Jang, S.Y. Kim and S.H. Ahn, *J. Alloys Compd.*,

- 2021, **889**, 161674.
- 43 M.H. Wang, Z.X. Lou, X.F. Wu, Y.W. Liu, J.Y. Zhao, K.Z. Sun, W.X. Li, J.C. Chen, H.Y. Yuan, M.H. Zhu, S. Dai, P.F. Liu and H.G. Yang, *Small*, 2022, **18**, 2200303.
- 44 S.C. Zignani, M.L. Faro, S. Trocino and A.S. Aricò, *Energies*, 2020, **13**, 1720.
- 45 X. Wu and K. Scott, *J. Power Sources*, 2012, **206**, 14–19.
- 46 X. Wu and K. Scott, *Int. J. Hydrogen Energy*, 2013, **38**, 3123–3129.
- 47 J.F. Chang, G.Z. Wang, A. Belharsa, J.J. Ge, W. Xing and Y. Yang, *Small Methods*, 2020, **4**, 1900632.
- 48 G. Assat and J.-M. Tarascon, *Nat. Energy*, 2018, **3**, 373–386.
- 49 M.N. Grisolia, J. Varignon, G. Sanchez-Santolino, A. Arora, S. Valencia, M. Varela, R. Abrudan, E. Weschke, E. Schierle, J.E. Rault, J. P. Rueff, A. Barthélémy, J. Santamaria and M. Bibes, *Nat. Phys.*, 2016, **12**, 484–492.
- 50 A.V. Ushakov, S.V. Streltsov and D.I. Khomskii, *J. Phys.: Condens. Matter*, 2011, **23**, 445601.
- 51 W.T. Hong, K.A. Stoerzinger, Y.-L. Lee, L. Giordano, A. Grimaud, A.M. Johnson, J. Hwang, E.J. Crumlin, W. Yang and Y. Shao-Horn, *Energy Environ. Sci.*, 2017, **10**, 2190–2200.
- 52 J. Zaanen, G.A. Sawatzky and J.W. Allen, *Phys. Rev. Lett.*, 1985, **55**, 418–421.
- 53 A. Grimaud, W.T. Hong, Y. Shao-Horn, J.M. Tarascon, *Nat. Mater.*, 2016, **15**, 121.
- 54 Y. Zhu, H.A. Tahini, Z. Hu, Z.-G. Chen, W. Zhou, A.C. Komarek, Q. Lin, H.-J. Lin, C.-T. Chen, Y. Zhong, M.T. Fernández-Díaz, S.C. Smith, H. Wang, M. Liu and Z. Shao, *Adv. Mater.*, 2020, **32**, 1905025.
- 55 E. Fabbri and T.J. Schmidt, *ACS Catal.*, 2018, **8**, 9765–9774.
- 56 N. Li, D.K. Bediako, R.G. Hadt, D. Hayes, T.J. Kempa, F. von Cube, D.C. Bell, L.X. Chen and D.G. Nocera, *Proc. Natl. Acad. Sci. U. S. A.*, 2017, **114**, 1486–1491.
- 57 P.D. Lukovtsev and G.J. Slaidin, *Electrochim. Acta*, 1962, **6**, 17–21.



- 58 M. Louër, D. Louër and D. Grandjean, *Acta Cryst.*, 1973, **B29**, 1696–1703.
- 59 L. Eriksson, D. Louër and P.E. Werner, *Journal of Solid State Chemistry*, 1989, **81**, 9–20.
- 60 S.L. Zhao, Y. Wang, J.C. Dong, C.T. He, H.J. Yin, P.F. An, K. Zhao, X.F. Zhang, C. Gao, L.J. Zhang, J.W. Lv, J.X. Wang, J.Q. Zhang, A.M. Khattak, N.A. Khan, Z.X. Wei, J. Zhang, S.Q. Liu, H.J. Zhao and Z.Y. Tang, *Nat. Energy*, 2016, **1**, 16184.
- 61 J. Jiang, F.F. Sun, S. Zhou, W. Hu, H. Zhang, J.C. Dong, Z. Jiang, J.J. Zhao, J.F. Li, W.S. Yan and M. Wang, *Nat. Commun.*, 2018, **9**, 2885.
- 62 J.Y.C. Chen, L. Dang, H.F. Liang, W.L. Bi, J.B. Gerken, S. Jin, E. Ercan Alp and Shannon S. Stahl, *J. Am. Chem. Soc.*, 2015, **137**, 15090–15093.
- 63 T. Ouyang, X.T. Wang, X.Q. Mai, A.N. Chen, Z.Y. Tang and Z.Q. Liu, *Angew. Chem. Int. Ed.*, 2020, **59**, 11948–11957.
- 64 J.G. Lee, J. Hwang, H.J. Hwang, O.S. Jeon, J. Jang, O. Kwon, Y. Lee, B. Han and Y.G. Shul, *J. Am. Chem. Soc.*, 2016, **138**, 3541–3547.
- 65 X. Li, H. Wang, Z.M. Cui, Y.T. Li, S. Xin, J.S. Zhou, Y.W. Long, C.Q. Jin and J.B. Goodenough, *Sci. Adv.*, 2019, **5**, eaav6262.
- 66 Z.F. Huang, J.J. Song, Y.H. Du, S.B. Xi, S. Dou, J.M.V. Nsanzimana, C. Wang, Z.C.J. Xu and X. Wang, *Nat. Energy*, 2019, **4**, 329–338.
- 67 A. Grimaud, O. Diaz-Morales, B.H. Han, W.T. Hong, Y.-L. Lee, L. Giordano, K.A. Stoerzinger, M.T.M. Koper and Y. Shao-Horn, *Nat. Chem.*, 2017, **9**, 457–465.
- 68 X.M. Xu, Y.L. Pan, Y.J. Zhong, C.L. Shi, D.Q. Guan, L. Ge, Z.W. Hu, Y.Y. Chin, H.J. Lin, C.T. Chen, H. Wang, S.P. Jiang and Z.P. Shao, *Adv. Sci.*, 2022, **9**, 2200530.
- 69 J.L. Xia, H.Y. Zhao, B.L. Huang, L.L. Xu, M. Luo, J.W. Wang, F. Luo, Y.P. Du and C.H. Yan, *Adv. Funct. Mater.*, 2020, **30**, 1908367.
- 70 Y. Liu, Z. Wang, J.P.M. Veder, Z. Xu, Y. Zhong, W. Zhou, M.O. Tade, S. Wang and Z. Shao,

*Adv. Energy Mater.*, 2018, **8**, 1702604.

71 B.L. Tian, H. Shin, S.T. Liu, M.C. Fei, Z.Y. Mu, C. Liu, Y.H. Pan, Y.M. Sun, W.A. Goddard,  
and M.N. Ding, *Angew. Chem. Int. Ed.*, 2021, **60**, 16448–16456.